



# The stellar bar – dark matter halo connection in the TNG50 simulations

SIOREE ANSAR <sup>1,2</sup> AND MOUSUMI DAS <sup>1</sup>

<sup>1</sup>Indian Institute of Astrophysics, Bangalore 560034, India

<sup>2</sup>Pondicherry University, R.V. Nagar, Kalapet 605014, Puducherry, India

## ABSTRACT

Stellar bars in disk galaxies grow by losing angular momentum to their environments, including the Dark Matter (DM) halo, stellar and gas disks, and interacting satellite galaxies. This exchange of angular momentum during galaxy evolution hints at a connection between bar properties and the DM halo spin  $\lambda$  – the dimensionless form of DM angular momentum. We investigate the connection of halo spin  $\lambda$  and galaxy properties in the presence/absence of stellar bars, using the cosmological magneto-hydrodynamic TNG50 simulations at three redshifts  $z_r = 0, 0.1$  and 1. We estimate the halo spin for barred and unbarred galaxies (bar strength:  $0 < A_2/A_0 < 0.7$ ) at the central regions of the DM halo close to the galaxy disk and far from the disk, close to halo virial radius. At  $z_r = 0$ , strongly barred galaxies ( $A_2/A_0 > 0.4$ ) reside in DM halos having low spin and low specific angular momentum, while unbarred and weakly barred galaxies ( $A_2/A_0 < 0.2$ ) are hosted in high spin and high specific angular momentum halos. The inverse correlation between bar strength and halo spin is surprising since previous studies show that bars transfer angular momentum to DM halos. However, the bar strength-halo spin connection is more complex at higher redshift ( $z_r = 1$ ) with higher halo spin for all galaxies than that at  $z_r = 0$ . Using galaxy samples across various DM halo mass ranges, we highlight the importance of sample selection in obtaining meaningful results. Investigating the bar-halo connection in further detail is crucial for understanding the impact of bars on galaxy evolution models.

*Keywords:* galaxies: haloes – galaxies: bar – cosmology: dark matter – software: simulations

## 1. INTRODUCTION

Barred galaxies constitute a major fraction of the disk galaxy population in our local Universe. Studies using controlled galaxy simulations and cosmological simulations have shown that DM halo plays an important role in the formation of bar instability and in the evolution of bar in the stellar disk of galaxies (Efstathiou et al. 1982; Ostriker & Peebles 1973; Marioni et al. 2022; Ansar et al. 2023b). While the study of bar and DM halo interaction using isolated controlled galaxy simulations has the advantage of tracking specific dynamical processes, for example, angular momentum transfer between the disk and the halo (see Sellwood (2014) for a detailed review), cosmological simulations provide a scope to study bars in galaxies that form and evolve in a cosmological

environment, undergoing multiple satellite interactions, flyby events, gas in-fall and outflow events, star formation and stellar feedback in the disk, along with a central supermassive black hole and a co-evolving DM halo. Cosmological simulations can also help probe the interaction between the disk and the DM halo at different redshifts, which can help us understand the evolution of the bar – DM halo interaction in the observable Universe.

The properties of the DM halos at redshift  $z_r = 0$ , such as the DM density and DM angular momentum, are the result of the nonlinear evolution of the initial matter density field in the presence of tidal torques (Peebles 1969; Doroshkevich 1970; White 1984; Barnes & Efstathiou 1987; Schäfer 2009) as well as mergers and interactions with multiple satellite galaxies (Maller et al. 2002; Vitvitska et al. 2002; Bett & Frenk 2016; Rodriguez-Gomez et al. 2017). The DM halo angular momentum is often expressed in a dimensionless form, referred to as the DM halo spin  $\lambda$ . The halo spin at the

Corresponding author: Sioree Ansar  
sioree.ansar@iiap.res.in, sioreeansar@gmail.com

virial radius ( $r_{vir}$ ) is given by the Bullock et al. (2001) halo spin parameter ( $\lambda_B = L/\sqrt{2}M_{vir}r_{vir}v_c(r_{vir})$ <sup>1</sup>) that is derived from the general expression of halo spin parameter defined by Peebles (1969)<sup>2</sup>:

$$\lambda = \frac{L|E|^{1/2}}{GM^{5/2}} \quad (1)$$

where  $L$  is the total angular momentum of the halo,  $E$  is the total energy and  $M$  is the mass of the DM halo within radius  $r$ .

Investigating the properties of halo spin and its connection with galaxy properties has been of interest in many studies (Bett et al. 2007, 2010; Bett & Frenk 2012, 2016). Halo spin plays an important role in galaxy sizes – faster-rotating halos having higher halo spins are associated with larger disks (Kim & Lee 2013; Jiang et al. 2019; Rodriguez-Gomez et al. 2022; Pérez-Montaño et al. 2022; Yang et al. 2023). Romeo et al. (2023) studied a large sample of barred S0 galaxies to find out the connection between halo spin, disk spin and bar structure. Zjupa & Springel (2017) found that the halo spin (both  $\lambda_B$  and  $\lambda_P$  at  $r_{vir}$ ) does not get affected much by the collapse of the baryons in DM halos. Recently, Rosas-Guevara et al. (2022) using current cosmological hydrodynamical TNG50 simulations (Nelson et al. 2019; Pillepich et al. 2019) showed that the halo spin (at  $r_{vir}$ ;  $\lambda_B$ ) of barred galaxies is lower than the unbarred galaxies at redshift  $z_r = 0$  (also see Izquierdo-Villalba et al. 2022). However, there has been no comprehensive study on the origin of the trend between bar strength and halo spin/halo angular momentum.

Studies using controlled and isolated galaxy simulations have found different trends of the DM halo properties that aid the formation of bars. Athanassoula & Misiriotis (2002) showed that galaxies with higher DM concentration (having similar stellar to DM ratio) grow stronger, thinner and longer bars due to the transfer of angular momentum from the disk to the DM halo at resonances (Athanassoula 2002). A central mass concentration in the form of a stellar bulge or a centrally concentrated DM halo can inhibit bar formation (Ostriker & Peebles 1973; Saha & Naab 2013; Kataria & Das 2018; Jang & Kim 2023). Apart from the nature of the DM halo profile, the angular momentum distribution in the central regions of galaxies also plays a major role in bar formation (Long et al. 2014; Collier et al. 2018, 2019a,b; Collier & Madigan 2021) and the time

of bar buckling (Long et al. 2014; Collier et al. 2018; Kataria & Shen 2022; Li et al. 2023a,b).

Recently Li et al. (2023a) studied the evolution of bars in spinning DM halos with varying central densities. For high spinning halos (at  $r_{vir}$ ), they find a significantly large time interval between bar formation and bar buckling, during which the bar strength and pattern speed are constant and the stellar bar aligns with the DM bar and does not transfer angular momentum to the DM halo. However, bar formation is more likely to be affected by the inner halo spin/angular momentum close to the disk rather than at large radii, far from the disk (Kataria & Shen 2022; Ansar et al. 2023a).

A connection between DM halo spin and the presence of a bar is based on the transfer of angular momentum transport from the disk to the DM halo through the gravitational interaction of the bar (Debattista & Sellwood 2000; Athanassoula 2002; Athanassoula & Misiriotis 2002), thereby increasing the angular momentum of the DM halo. However, the net increase of angular momentum of the DM halo due to the bar–halo interaction is unclear in a cosmologically evolving system, as several other external processes (e.g., satellite mergers) can equally contribute to the change in angular momentum of the DM halo and the disk.

In this article, we investigate the connection between the DM halos and stellar bars of disk galaxies in the TNG50 cosmological magneto-hydrodynamical simulation (Nelson et al. 2019; Pillepich et al. 2019). We examine galaxies of different bar strengths (Section 2.1), at different halo radii of the host DM halo and at multiple redshifts. We investigate the origin of this anti-correlation by studying high redshift galaxy samples. Additionally, we investigate whether other properties of the DM halo and the baryonic disk are similarly correlated to the dark matter properties in these galaxies.

We structure this article as follows. We introduce the TNG50 simulations and the galaxy samples in Section 2. We discuss the halo spin of the barred and unbarred galaxies of comparable mass in Section 3 and for the whole sample of galaxies in Section 4. In Section 4 we examine the other DM halo properties and stellar and gas disk properties of our sample and in Section 5 we discuss our findings. We present our conclusions in Section 6.

## 2. TNG50 SIMULATIONS AND GALAXY SAMPLE

We select large samples of galaxies from the cosmological magneto-hydrodynamical simulations Illus-

<sup>1</sup> Where  $L$ ,  $M_{vir}$  and  $v_c(r_{vir})$  is the total halo angular momentum, halo mass and circular velocity at  $r_{vir}$ .

<sup>2</sup>  $\lambda_P$  is known as the Peebles (1969) halo spin at virial radius.

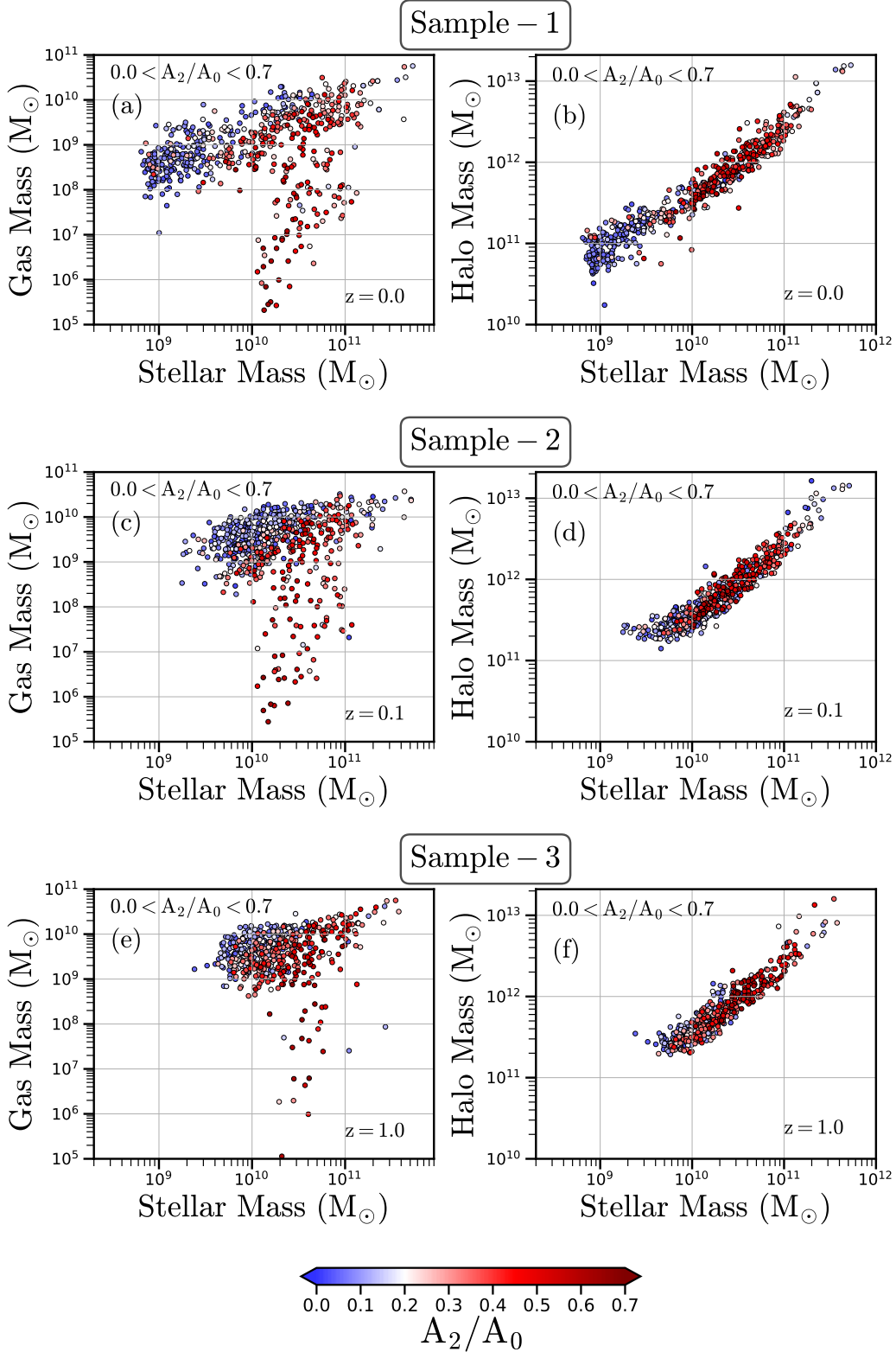


Figure 1. The stellar mass, gas disk mass (panel a, c and e) and dark matter halo mass (panel b, d and f) of the galaxies in our sample at redshift  $z_r = 0.0$  (top row),  $0.1$  (middle row) and  $1.0$  (bottom row) with varied bar strengths (in color). In all panels the bar strength is color-coded with blue for low bar strength  $A_2/A_0 < 0.2$  (see Section 2.1), red for high bar strength  $A_2/A_0 > 0.2$  and white for  $A_2/A_0 = 0.2$ . In panels a, c and e, a large number of galaxies show low gas content, although most of them have rotationally supported stellar disks.

trisTNG<sup>3</sup> (The Next Generation) (Weinberger et al. 2017; Pillepich et al. 2018) that is run using the moving mesh code AREPO (Springel 2010). We use one of the highest resolution data sets TNG50 (Nelson et al. 2019; Pillepich et al. 2019), having a volume of  $\sim (51 \text{ Mpc})^3$  and an average mass resolution of  $8 \times 10^4 M_\odot$  for the baryonic particles and  $4.5 \times 10^5 M_\odot$  for the dark matter particles.

We use the pre-computed estimates of dark matter halo mass, stellar disk mass and gas disk mass from the TNG website (Nelson et al. 2019; Pillepich et al. 2019). We adopt the dark matter halo mass from `SubhaloMassType` which accounts for the total mass of all the particles contained in a Subhalo, and the stellar and gas disk mass using `SubhaloMassInRadType` parameter which provides the aggregate of masses of all particles (stars or gas) within twice the stellar half-mass radius. Using the above mass definitions, we form an initial galaxy sample of 1892, 1758 and 1531 galaxies from the TNG50 data set at redshift  $z = 0, 0.1$  and  $1.0$ , in the galaxy stellar mass range of  $10^9 < M_*/M_\odot < 10^{12}$  and dark matter halo mass in the range of  $10^{10} < M_*/M_\odot < 2 \times 10^{13}$  containing both barred and unbarred galaxies.

From the above samples, we choose disk galaxies from visual inspection and remove the galaxies that show large deformation in the stellar disk due to ongoing mergers/flyby events of satellites or galaxies that show enhanced off-center star formation in the central region that can be misinterpreted as a stellar bar by the bar strength (Section 2.1). We avoid galaxies having too less star particles to resolve the central region of the disk. Following the above criteria, we select barred and unbarred disk galaxies from the above samples, with 597 galaxies at redshift  $z_r = 0$ , 650 galaxies at  $z_r = 0.1$  and 509 galaxies at  $z_r = 1.0$ . Note that, we do not track the progenitors of the galaxies at higher redshifts but construct independent samples of galaxies at the three redshifts.

### 2.1. Barred and unbarred galaxies

To find the barred galaxies we first project the disk galaxies in the face-on orientation on the x-y Cartesian coordinate plane such that the maximum angular momentum of the disk is towards the positive z-axis. We rotate the whole system including the gas particles and dark matter particles accordingly in the same orientation. Once we have the galaxy disks and the corresponding dark matter halo in the required orientation (with the disk lying in the x-y plane), we use the Fourier de-

composition method to identify the triaxial barred structures in the three galaxy samples at different redshifts.

We decompose the face-on stellar surface density  $\Sigma_*(r)$  into Fourier modes  $\Sigma_{m=0}^\infty A_m(r) \exp(im\phi_m)$ . The ratio of the amplitude of the  $m = 2$  and  $m = 0$  Fourier mode is the bar strength (Athanasoula 2003), given as:

$$\frac{A_2}{A_0} = \frac{\sqrt{a_2^2 + b_2^2}}{\Sigma_{j=0}^N m_{*,j}} \quad (2)$$

where in general for the  $m^{\text{th}}$  mode,  $a_m = \Sigma_{i=1}^N m_{*,i} \cos(m\theta_i)$ ,  $b_m = \Sigma_{i=1}^N m_{*,i} \sin(m\theta_i)$ ,  $\theta_i$  is the azimuthal coordinate,  $m_{*,j}$  is the mass of the  $j^{\text{th}}$  star particle,  $N$  is the total number of star particles between the radius  $r$  to  $r + \Delta r$ . We adopt  $\Delta r = 200 \text{ pc}$ . The criteria most frequently used in the literature to differentiate between barred and unbarred galaxies is based on the bar strength:  $A_2/A_0 > 0.2$  for barred galaxies and  $A_2/A_0 \leq 0.2$  for weakly barred and unbarred galaxies. We note that our sample has a slightly larger number of barred galaxies compared to the number of unbarred galaxies. According to the above definition of bar strength, the bar fraction (fraction of galaxies hosting a bar) is 0.54 at  $z_r = 0$ , 0.44 at  $z_r = 0.1$  and 0.54 at  $z_r = 1.0$ .

In Figure 1, we show the stellar mass, gas mass and DM halo mass of the galaxies from the three samples at  $z_r = 0.0, 0.1$  and  $1.0$ , along with their peak bar strength  $A_2/A_0|_{\text{max}}$  in the central region of the disk ( $r < 5 \text{ kpc}$ ) in color (colorbar range:  $0.0 < A_2/A_0|_{\text{max}} < 0.7$ ). Barred galaxies with strength  $A_2/A_0|_{\text{max}} > 0.2$  are in shades of red and the unbarred galaxies with strength  $A_2/A_0|_{\text{max}} < 0.2$  are in shades of blue and white color is for  $A_2/A_0|_{\text{max}} \sim 0.2$ .

We divide the galaxies into 7 groups of different bar strengths between  $A_2/A_0|_{\text{max}} = 0.0-0.7$ , as in Table 1, where we present the number of galaxies in each bar strength interval ( $\Delta A_2/A_0|_{\text{max}} = 0.1$ ), for three different redshifts  $z_r = 0.0, 0.1$  and  $1.0$ . We present the stellar mass, gas mass and DM halo mass of the galaxies at  $z_r = 0$  in each of the seven bar strength intervals separately in Figure 8 in Appendix A. The number of barred galaxies decreases for higher bar strengths and the strongest bars ( $A_2/A_0|_{\text{max}} > 0.6$ ) lie in the stellar mass range of  $10^{10}-10^{11} M_\odot$  for all three redshifts. On a side note, in Figure 1 (panel a, c and e), the number of barred and unbarred galaxies within stellar mass  $10^{10} < M_*/M_\odot < 3 \times 10^{11}$  and with low gas content, increases for lower redshifts, which distinctly appear as a separate group of points in each panel. We defer the detailed study of the loss of gas content galaxies to a separate article, the cause of which may be due to multiple processes during evolution, for example, high star for-

<sup>3</sup> <https://www.tng-project.org/>

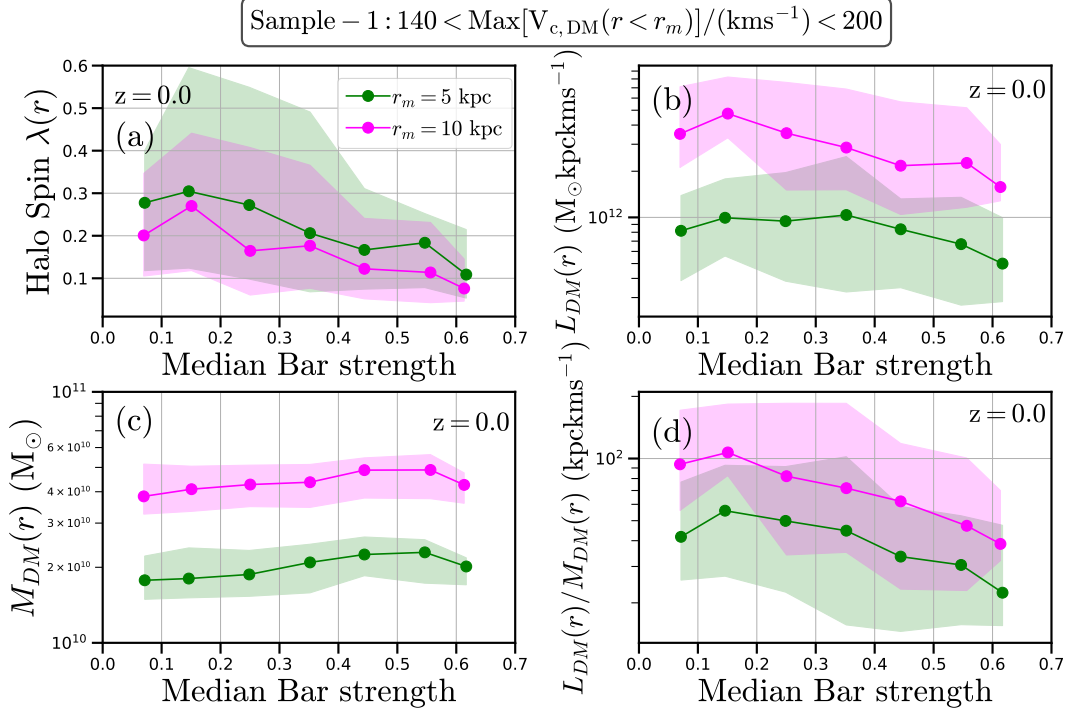


**Figure 2.** The anti-correlation between bar strength and dark matter halo properties at redshift  $z_r = 0.0$ . Figure shows the median halo spin (panel a), median DM angular momentum (panel b), median DM mass (panel c) and median specific angular momentum of DM (panel d) for each of the bar strength groups from Table 1 at redshift  $z_r = 0$ , for two radii,  $r_m = 5$  kpc (green), 10 kpc (magenta), in the velocity range  $140 < \text{Max}[V_{c,DM}(r < r_m)]/(\text{kms}^{-1}) < 200$ . The solid circles denote the median values and the shaded regions are bounded by the 16<sup>th</sup> and 84<sup>th</sup> percentile curves.

**Table 1.** TNG50 galaxies of different bar strength at redshift  $z_r = 0, 0.1$  and 1.0.

Bar Strength*	Sample 1	Sample 2	Sample 3
$(A_2/A_0)_{max}$ range	$(z_r = 0)$	$(z_r = 0.1)$	$(z_r = 1.0)$
(1)	(2)	(3)	(4)
0.0-0.1	201	224	111
0.1-0.2	72	137	121
0.2-0.3	107	90	68
0.3-0.4	95	78	98
0.4-0.5	74	70	54
0.5-0.6	38	38	41
0.6-0.7	10	13	16

NOTE— Columns: 1. Bar strength  $(A_2/A_0)_{max}$  (see Section 2.1); 2. Number of galaxies at redshift  $z_r = 0$ ; 3. Number of galaxies at redshift  $z_r = 0.1$ ; 4. Number of galaxies at redshift  $z_r = 1$ . A large number of low bar strength galaxies reflects the high number of low mass galaxies where the bar formation is not effective due to reasons like low stellar surface density and high stellar dispersion, shallow DM potential.

mation, ram-pressure stripping of gas from these galaxies, and satellite interactions. We also note a significant number of low mass ( $M_* \sim 10^9 M_\odot$ ) unbarred galaxies (blue) at redshift  $z_r = 0$ , which are missing from the higher redshift samples (also see Table 1).

### 3. HALO SPIN OF BARRED AND UNBARRED GALAXIES OF COMPARABLE HALO MASS

#### 3.1. At redshift $z_r = 0$

We aim to study the halo spin of barred and unbarred galaxies having similar mass profiles of their DM halos at the central region close to the baryonic disk. We use the circular velocity  $V_{c,DM}(r) = \sqrt{GM_{DM}(r)/r}$  of the DM component to select galaxies with similar DM halo mass profiles ( $M_{DM}(r)$ ). We use the selection criteria of  $140 < \text{Max}[V_{c,DM}(r < r_m)]/(\text{kms}^{-1}) < 200$  at radius  $r_m = 5$  and 10 kpc, on each of the seven bar strength groups at  $z_r = 0$  from Table 1, as it maximises the number of galaxies following this selection criterion. At  $z_r = 0$ , we find 25, 21, 42, 34, 29, 29, and 10 galaxies at  $r_m = 10$  kpc and 19, 22, 48, 44, 45, 33 and 9 galaxies at  $r_m = 5$  kpc for each of the bar strength intervals from Table 1. Except for the highest bar strength bin ( $0.6 < A_2/A_0 < 0.7$ ), all other bar strength intervals have a moderate number of galaxies. In Figure 2, we



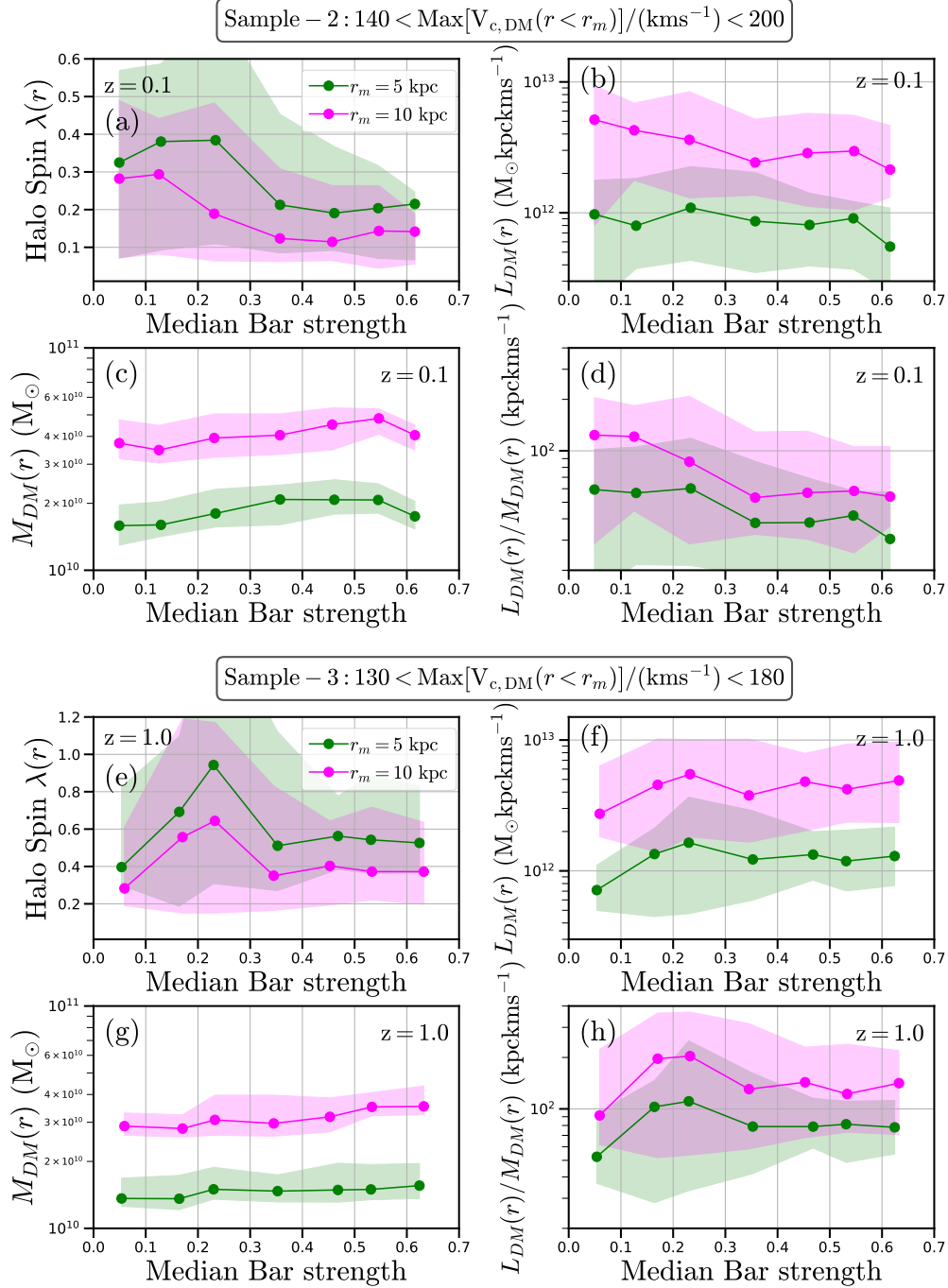


**Figure 3.** The connection between bar strength and dark matter halo properties at high redshift  $z_r = 0.1$  (panel a-d) and  $1.0$  (panel e-h). Same as Figure 2, for the velocity range:  $140 < \text{Max}[V_{c,DM}(r < r_m)]/(\text{kms}^{-1}) < 200$  at  $z_r = 0.1$  and  $130 < \text{Max}[V_{c,DM}(r < r_m)]/(\text{kms}^{-1}) < 180$  at  $z_r = 1.0$ . At  $z_r = 1.0$ , the bar strength – halo spin connection is more complex.

present the median halo spin (panel a), median angular momentum (panel b), median DM mass (panel c) and the median specific angular momentum (panel d) within  $r_m = 5$  (green) and 10 kpc (magenta), of the galaxies in the above sub-samples, with the median bar strength in the x-axis of each panel. The circular points connected with lines show the median values of each of the above quantities and shaded regions are bounded by 16<sup>th</sup> and 84<sup>th</sup> percentile curves.

In Figure 2, we observe that the median mass of the dark matter halos within  $r_m = 5$  and 10 kpc is nearly constant (panel c), while the median halo spin, the median angular momentum and the median specific angular momentum (panel b, c and d) decreases for galaxies with higher bar strength. For the unbarred and weakly barred galaxies ( $0 < A_2/A_0 < 0.2$ ) the median DM halo spin is higher, with a large spread in halo spin evident from the shaded regions. However, for the barred galaxies ( $0.2 < A_2/A_0 < 0.7$ ) the median halo spin decreases gradually and the spread in the spin values (width of shaded regions) also decreases. Additionally, the overall value of halo spin decreases for higher radii in each of the bar strength intervals, as previously observed in Ansar et al. (2023a).

The decrease in median halo spin is also the reflection of the decrease in median angular momentum and median specific angular momentum of the DM halo for galaxies with higher bar strengths. We note that there is a slight increase in the halo mass towards the high bar strength end. However, such a small change in mass will not be the major reason for the overall trend of decrease in halo angular momentum over the whole bar strength range.

For higher velocity ranges of DM circular velocity, for example,  $200 < \text{Max}[V_{c,DM}(r < r_m)]/(\text{kms}^{-1}) < 250$  at the same radii  $r_m = 5$  and 10 kpc, we find a similar trend of decrease in median halo spin, angular momentum and specific angular momentum (see Figure 9 in Appendix B). For a lower velocity range (e.g.,  $100 < \text{Max}[V_{c,DM}(r < r_m)]/(\text{kms}^{-1}) < 150$ ) we do not find a uniform mass distribution of galaxies for each of the bar strength intervals, and we cannot compare the halo spin for different bar strength intervals for the lower mass sample (see Figure 10 in Appendix B). However, we note that for the low-mass galaxies, the majority of the unbarred galaxies have low DM halo spin, which can decrease the median spin value significantly if we relax the criteria of comparable DM halo mass, as seen in the following Section 4.1.

### 3.2. At higher redshift $z_r = 0.1$ and 1.0

Even if there is an anti-correlation between the DM halo spin and the bar strength at redshift  $z_r = 0$ , does the inverse relation hold at higher redshifts? To answer this question we examine the barred and unbarred galaxies at higher redshifts  $z_r = 0.1$  and 1.0 by forming samples of similar halo mass galaxies from Table 1. We apply the selection criteria of  $140 < \text{Max}[V_{c,DM}(r < r_m)]/(\text{kms}^{-1}) < 200$ , on each of the seven bar strength groups at  $z_r = 0.1$  (Sample-2) to find 37, 58, 46, 39, 40, 28 and 12 galaxies at  $r_m = 10$  kpc and 37, 40, 42, 42, 49, 34, 12, galaxies at  $r_m = 5$  kpc. At higher redshift  $z_r = 1.0$ , we do not obtain a sufficient number of galaxies in Sample-3 in the above circular velocity range. Hence we use a slightly different velocity selection criteria of  $130 < \text{Max}[V_{c,DM}(r < r_m)]/(\text{kms}^{-1}) < 180$  for  $z_r = 1.0$  to find 18, 24, 16, 39, 33, 32 and 14 galaxies for  $r_m = 10$  kpc and 8, 12, 12, 24, 30, 35 and 15 galaxies for  $r_m = 5$  kpc. We estimate the median halo spin, median halo angular momentum, median halo mass and median halo specific angular momentum for each of the seven bar strength groups in Sample-2 and Sample-3 (similar to Sample-1) and present it in Figure 3 (similar to Figure 2).

In Figure 3 (panels a–d), we find that at a slightly higher redshift than present ( $z_r = 0.1$ ) the halo spin and bar strength follow a similar inverse correlation as in the case of redshift  $z_r = 0$ . However, the median halo spin in each bar strength interval is higher at  $z_r = 0.1$  as compared to  $z_r = 0$ . For example, for  $r_m = 5$  kpc, the median spin for the highest bar strength interval ( $0.6 < A_2/A_0 < 0.7$ ) is twice as large ( $\sim 0.2$ ) as the median spin for the same bar strength interval at  $z_r = 0$  ( $\sim 0.1$ ). While for the unbarred galaxies ( $0.1 < A_2/A_0 < 0.2$ ) the median halo spin is  $\sim 0.4$  at  $z_r = 0.1$  and  $\sim 0.3$  at  $z_r = 0.0$  (see Figure 2). The median halo mass is nearly constant over the bar strength intervals (see panel c), while the median halo angular momentum is nearly constant for  $r_m = 5$  kpc, but has a decreasing trend for  $r_m = 10$  kpc. The median specific angular momentum of the DM halo for both radii has similar decreasing trends with higher bar strengths (see panels b and d).

The inverse correlation between the median DM halo spin and the median bar strength is maintained at low redshifts ( $z_r = 0.0$  and 0.1), but it is not true for high redshift  $z_r = 1.0$  galaxies (see panels e–h in Figure 3). There are two major differences between the halo spins of high redshift and low redshift galaxies. First, the high redshift galaxies ( $z_r = 1.0$ ) have higher median halo spin values compared to the low redshifts ( $z_r = 0.0$  and 0.1) for nearly all bar strength ranges. This may be because the galaxies and their DM halos are not well settled and

have more chaotic motion of particles at higher redshifts. For comparison, at  $r_m = 5$  kpc, the median halo spin is  $\sim 0.6$  for the bar strength interval ( $0.6 < A_2/A_0 < 0.7$ ), while it is  $\sim 0.1$  at  $z_r = 0.0$ . Second, the halo spin for the high bar strength galaxies ( $0.3 < A_2/A_0 < 0.7$ ) and very low strength galaxies ( $A_2/A_0 < 0.1$ ) is nearly similar, however in the transition region of low to high bar strength galaxies ( $0.1 < A_2/A_0 < 0.3$ ) the halo spin increases to high values.

To summarise Section 3, the inverse correlation between median bar strength and median halo spin of galaxies at low redshift ( $z_r = 0.0, 0.1$ ) and a more complex relation at high redshift ( $z_r = 1.0$ ), indicate an underlying evolutionary process that is different for strongly barred galaxies and unbarred galaxies. We discuss the possible reasons for the evolution of halo spin in Section 5.

#### 4. HALO PROPERTIES OF ALL BARRED AND UNBARRED GALAXIES

In this Section, we investigate the barred and unbarred galaxy samples from TNG50 irrespective of the stellar or DM mass of the galaxy, i.e., we do not select a range of the constant circular velocity of DM as in the previous Section 3, but consider all the galaxies from the three samples in Table 1 irrespective of their DM halo mass. In Section 4.1 we investigate how the halo spin varies for different bar strength intervals and in Section 4.3 we study the variation of the other DM halo properties and baryonic disk properties of the three samples.

##### 4.1. Dark matter halo spin

Halo spin  $\lambda(r)$  can be estimated at different radii of the DM halo (Ansar et al. 2023a), other than the virial radius of the halo (Bullock et al. 2001). We estimate the halo spin at multiple radii of the DM halo, namely  $r = 5, 10$  and  $100$  kpc. We also estimate the halo spin close to the disk at  $R_{\star,60}$  and at  $R_{\star,90}$ , the radius at which the stellar mass reaches 60% and 90% of the total mass inside a spherical region (centered at disk center) of radius 30 kpc. To estimate  $R_{\star,X}$ , we choose a maximum radius of 30 kpc as all of the galaxies in our sample are well within the 30 kpc radius. We investigate the issue of numerical relaxation (Power et al. 2003) and consider only those galaxies which fulfil numerical convergence. See Appendix C) for more details on how we avoid the effects of numerical relaxation at small radii in our sample galaxies. More than 77% (99%) of our sample galaxies show numerical convergence for  $r = R_{\star,60}$  at  $z_r = 0.0$  ( $z_r = 1.0$ ). At  $r = R_{\star,90}$ , 100% of our sample galaxies show numerical convergence. While we estimate the DM halo properties at  $r = R_{\star,60}$ , our new galaxy samples consist of 460 galaxies at  $z_r = 0.0$ , 626 galaxies at

$z_r = 0.1$  and 505 galaxies at  $z_r = 1.0$ . The new galaxy sample is sufficiently large to investigate DM halo properties as a function of the bar strength of the galaxies. In addition, we estimate the halo spin at the virial radius  $R_{200}$ , far from the central disk and close to the disk at  $0.15R_{200}$  and  $0.05R_{200}$ , where we expect a greater impact of the disk on the surrounding DM particles. We have checked that for  $r = 0.05R_{200}$  all the galaxies show numerical convergence. We present the detailed method of estimation of each radius in Appendix C.

For low-mass galaxies having small sizes, the above mentioned radii are lower compared to the high-mass galaxies (see Figure 11 in Appendix C). Consequently, the halo spins for high-mass galaxies are estimated at larger radii compared to low-mass galaxies. Additionally, we note that at redshift  $z_r = 0.0$ , the number of massive galaxies is lower compared to the low mass galaxies (unlike the high redshift samples; see Figure 1). All the above factors can play an important role in the halo spin distribution of the samples.

In Figure 4 we present the median halo spins of the galaxies in different bar strength bins for the three samples from Table 1 at redshift  $z_r = 0.0$  (top row),  $0.1$  (middle row) and  $1.0$  (bottom row), and at different radii (in green, magenta and blue colors). Similar to Figure 2 panel a, we show the median halo spin (solid circles) for different bar strength intervals along with the shaded regions bounding the 16<sup>th</sup> and 84<sup>th</sup> percentile of the population. The different colors in each panel represent the different radii at which we estimate halo spin, with blue for the largest radii, magenta for the intermediate radii and green for the smallest radii.

At  $z_r = 0.0$  (Figure 4, top row), except at the very low bar strength interval ( $0 < A_2/A_0 < 0.1$ ), we observe an overall similar trend (as in Figure 2) of decrease in halo spin with higher bar strength for all the radii in different panels. In general, for larger radii, the median halo spin decreases for nearly all the bar strength intervals. Additionally, the spread in the halo spin distribution (shaded regions) is broader in the low bar strength intervals compared to the high bar strength intervals (similar to Section 3; see Figure 4). We also note the decrease in the median halo spin in the lowest bar strength interval ( $0 < A_2/A_0 < 0.1$ ) which is dominated by the low mass, low spin galaxies mentioned in Section 3 (see Figure 5).

The halo spin at higher redshifts (Figure 4, middle row and bottom row), for example at  $z_r = 1.0$  is very different from halo spin at  $z_r = 0.0$ , although the spin distribution at  $z_r = 0.1$  has more similarity with spin at  $z_r = 0.0$ . There is significantly less number of low-mass galaxies that settle into a disk in our high redshift samples and unlike  $z_r = 0.0$ , we observe



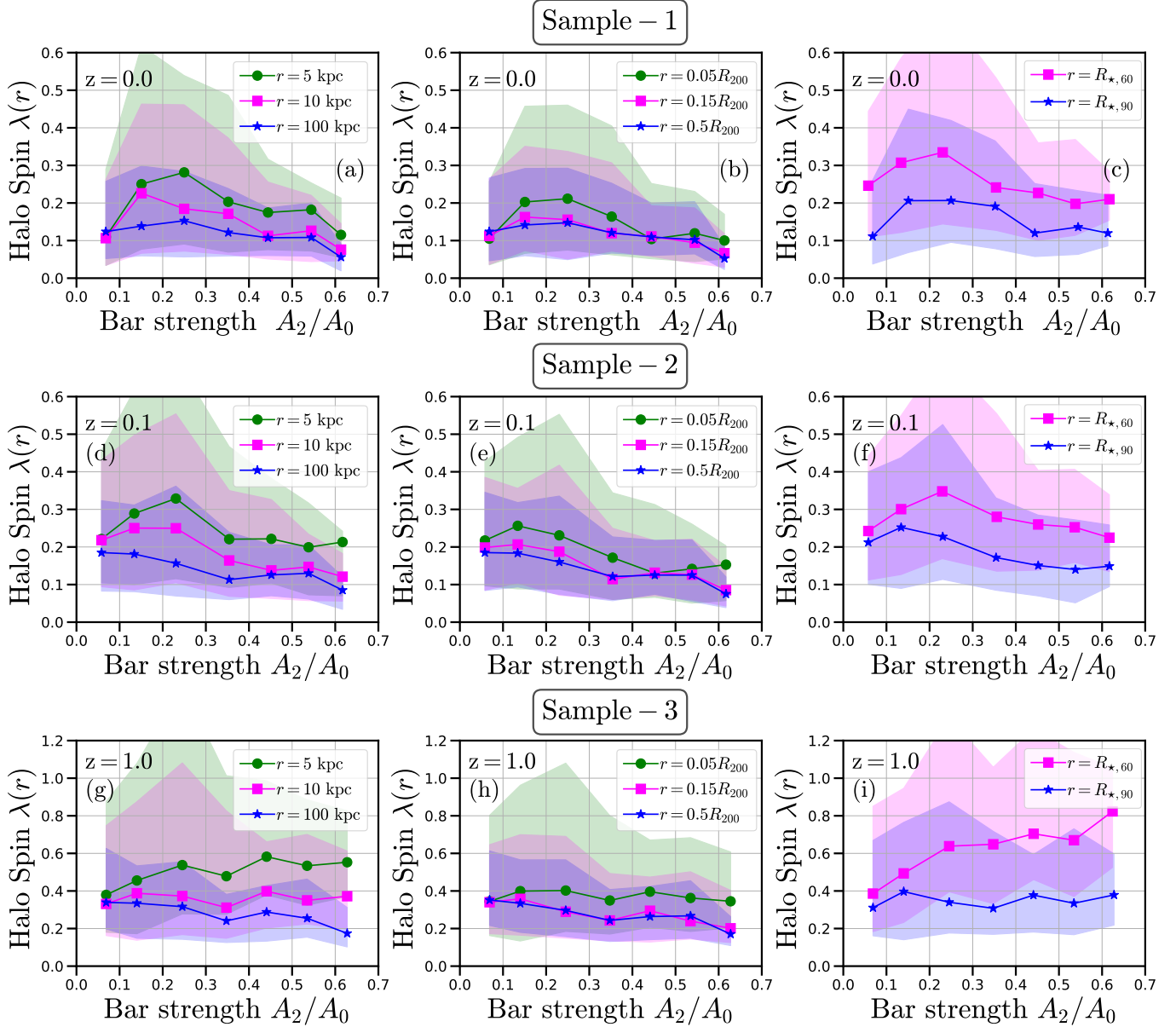


**Figure 4.** The connection between bar strength and dark matter halo spin at redshift  $z_r = 0.0$  (top row),  $0.1$  (middle row) and  $1.0$  (bottom row). Each panel shows the median halo spin and median bar strength (circles, squares and “ $\star$ ”) for each of the bar strength groups from Table 1, for different radii. In all panels, green circles are for the smallest radii, magenta squares are for the next radii and blue stars are for the largest radii, with the shaded regions of similar colors bounded by the 16<sup>th</sup> and 84<sup>th</sup> percentile curves of halo spin distribution. Left column shows halo spin at  $r = 5, 10$  and  $100$  kpc; middle column for  $r = 0.05R_{200}, 0.15R_{200}$  and  $0.5R_{200}$ ; the right column for  $r = R_{\star,60}$  and  $R_{\star,90}$  (see Section 4.1). At low redshift and small radii, the median halo spin decreases with increasing bar strength. The shape of the shaded regions highlights the skewed nature of the spin distribution in each bar strength group.

a higher median halo spin of the unbarred galaxies at  $z_r > 0.0$ . Overall, the halo spins for unbarred galaxies ( $0 < A_2/A_0 < 0.2$ ) are higher compared to the barred galaxies ( $0.2 < A_2/A_0 < 0.7$ ) even at  $z_r = 0.1$ . However, the low redshift trend does not hold at high redshift. At  $z_r = 1.0$ , the median halo spin close to the disk (green and magenta lines) is either similar for barred and unbarred galaxies or the trend reverses at very low radii

(green line in panel g; magenta line in panel i). At large radii, away from the disk (blue lines in panels g and h), the halo spin is higher for unbarred galaxies compared to barred galaxies.

The DM halo spin of the three galaxy samples at different redshifts indicates an evolutionary nature of halo spin that differs for the barred and unbarred galaxies.

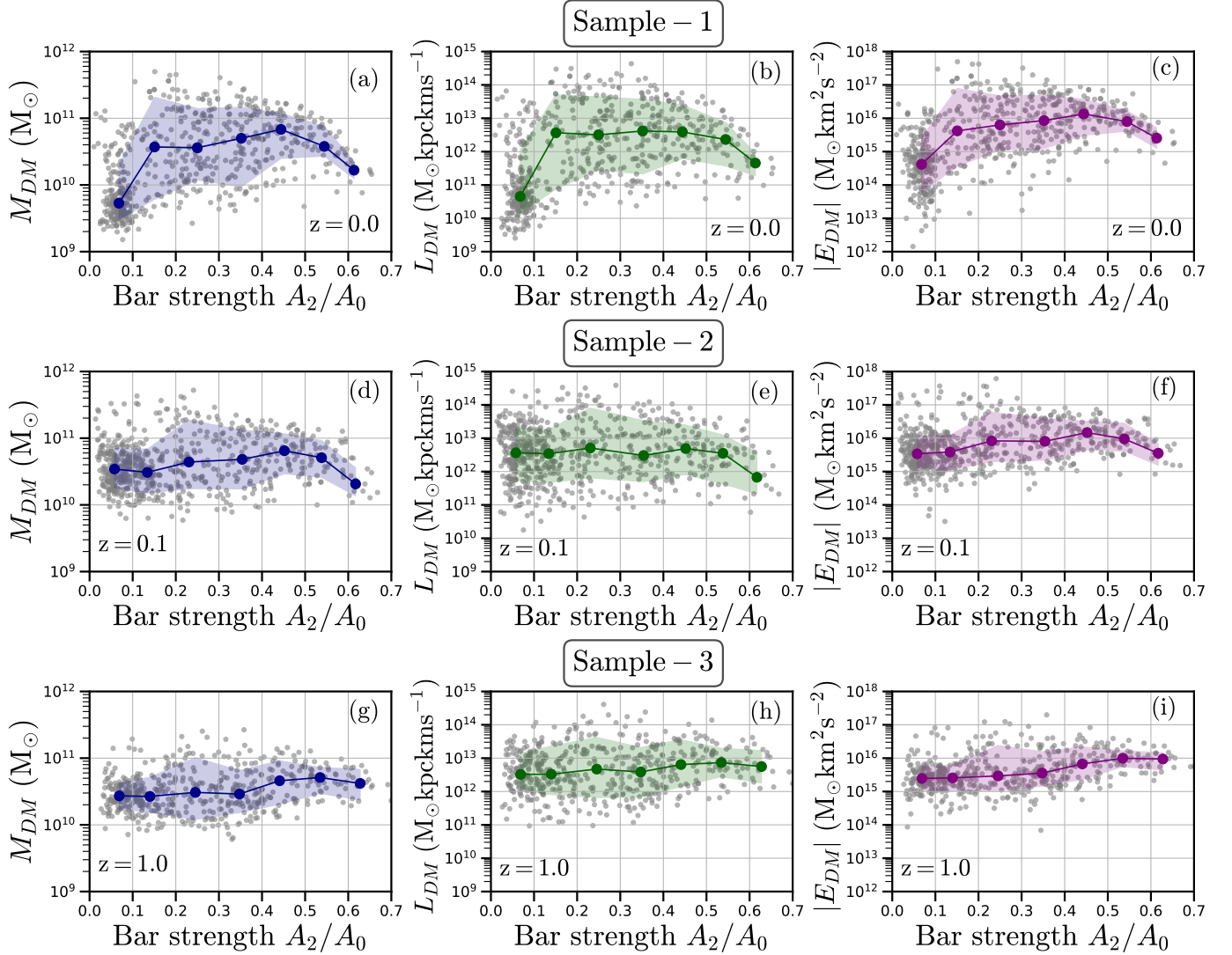


**Figure 5.** Dark matter halo mass (left column), angular momentum (middle column) and energy (right column) of the sample galaxies at redshifts  $z_r=0.0$  (top row),  $0.1$  (middle row) and  $1.0$  (bottom row), within spherical radius  $R_{*,90}$ . In each panel, grey points are values of each quantity divided into seven bar strength groups (Table 1). Blue, green and purple lines trace the median values in each bar strength group and the shaded regions show the 16<sup>th</sup> and 84<sup>th</sup> percentile of the sample. Each bar strength interval consists of DM halos with a wide range of mass, angular momentum and energy, however the scatter decreases at high redshifts.

#### 4.2. Other DM halo properties: Mass, Angular momentum and Energy

We examine the underlying properties of the dark matter halo — halo mass ( $M_{DM}$ ), halo angular momentum ( $L_{DM} = \sqrt{L_x^2 + L_y^2 + L_z^2}$ ) and halo energy ( $E_{DM}$ ) — for the three samples for which we estimate DM halo spin  $\lambda$  (Section 4.1). In Figure 5 we present the halo properties estimated within  $R_{*,90}$  for  $z_r = 0.0$  (top row),  $0.1$  (middle row) and  $1.0$  (bottom row). In three columns we show the total DM halo mass ( $M_{DM}$ ), the total angular momentum ( $L_{DM}$ ) and the absolute value of the total energy ( $|E_{DM}|$ ) for each of the galaxies in

the three samples with grey circles. We show the median values of the above properties in each bar strength group with blue, green and purple circles with shaded regions indicating the 16 percentile and 84 percentile of the distributions.

At  $z_r = 0.0$ , a large number of low mass halos ( $M_{DM}(R_{*,90}) < 10^{10} M_\odot$ ) is prominently seen in panel a of Figure 5 that have low angular momentum (panel b) and low energy (panel c). This population brings down the median value of halo spin for the unbarred galaxies ( $A_2/A_0 < 0.1$ ) in Figure 4 panel a. This low mass galaxy population is not present in the high redshift samples at  $z_r = 0.1$  (middle row) and  $1.0$  (bottom

row) and consequently the halo spin does not drop significantly for the unbarred galaxies at high redshifts. As we move from the low redshift Sample-1 to high redshift Sample-3, we find a more uniform distribution of DM halo mass, angular momentum and energy across the whole bar strength range ( $0.0 < A_2/A_0 < 0.7$ ). For example, at  $z_r = 1.0$  (panel g-i, Figure 5) the nearly constant median values of halo mass, angular momentum and energy are reflected in the nearly constant value of the median halo spin in panel i of Figure 4 (blue curve for  $r = R_{*,90}$ ). At low redshifts ( $z_r = 0.0$  and  $0.1$ ), the median mass, angular momentum and energy are not as uniform for the different bar strength bins as at high redshifts ( $z_r = 1.0$ ).

#### 4.3. Stellar disk and gas disk properties

In this Section, we investigate how the baryonic disk properties are connected to the presence of a bar in the disk of our galaxy samples. We study the properties of the stellar disk and the gas disk of the galaxies from the three samples from Table 1. We estimate the disk properties within a radius of  $R_{*,90}$  and  $R_{*,60}$ , introduced in Section 4.1. We find similar results for both radii. We present the results for  $r = R_{*,90}$  and mention the results for the radii  $r = R_{*,60}$  whenever there is a notable difference.

We estimate the stellar disk angular momentum ( $L_{*,tot}(r)$ ) from the vector sum of angular momentum of all the star particles within  $R_{*,90}$  and  $|z| < 2$  kpc. Similarly, for all the stars within the same volume ( $r < R_{*,90}$  and  $|z| < 2$  kpc), we estimate the stellar disk specific angular momentum in the  $z$ -direction ( $L_{*,z}(r)/M_*(r)$ ) and the ratio of the stellar dispersion to the stellar surface density ( $\sigma_*(r)/\Sigma_*(r)$ , proportional to disk instability parameter Toomre  $Q = \sigma_*(r)\kappa(r)/3.36G\Sigma_*(r)$ , where  $\kappa(r)$  is the epicyclic frequency). In Figure 6 we present the stellar disk properties —  $L_{*,tot}(r)$  (left column),  $L_{*,z}(r)/M_*(r)$  (middle column) and  $\sigma_*(r)/\Sigma_*(r)$  (right column)— for each galaxy in the three samples at three different redshifts  $z_r = 0.0$  (top row),  $0.1$  (middle row) and  $1.0$  (bottom row). We color code the stellar dispersion (within  $R_{*,90}$ ) for  $L_{*,tot}(r)$  and  $L_{*,z}(r)/M_*(r)$ , but not for  $\sigma_*(r)/\Sigma_*(r)$ .

At  $z_r = 0.0$  (top row of Figure 6), we observe a large spread in stellar disk angular momentum (panel a) and specific angular momentum (panel b), with a large number of low stellar mass population having low angular momentum and low stellar dispersion, for the unbarred galaxies ( $A_2/A_0 < 0.1$ ). As we move to higher redshift at  $z_r = 0.1$ , the scatter in  $L_{*,tot}(r)$  and  $L_{*,z}(r)/M_*(r)$  decreases and we observe a population of low dispersion stellar disks (not low stellar mass though) promi-

nently for the low bar strength galaxies ( $A_2/A_0 < 0.2$ ). At high redshift  $z_r = 1.0$  (bottom row), the scatter in  $L_{*,tot}(r)$  is even lower, with a uniform and nearly constant  $L_{*,z}(r)/M_*(r)$  across the whole bar strength range ( $0 < A_2/A_0 < 0.7$ ). The mean stellar dispersion for the high redshift galaxies is higher in Sample 3. However, other than the stellar dispersion in a galaxy the stellar surface density also plays an important role in balancing the pressure support in the disk. The last column in Figure 6 shows the ratio  $\sigma_*(r)/\Sigma_*(r)|_{(r < R_{*,90})}$  for all the galaxies in the three samples and indicates similar trend of low bar strength galaxies having higher value compared to high bar strength galaxies for the three redshifts  $z_r = 0.0, 0.1$  and  $1.0$ . However, we have to be *careful* in inferring trends in  $\sigma_*(r)/\Sigma_*(r)$  (or Toomre  $Q$ ) at different radii for different bar strengths, as it depends on the choice of the radii. At the central regions of the disk, close to the bar, the measure of Toomre  $Q$  may be related to the formation of a bar instability.

We also investigate the stellar mass fraction, the DM mass fraction and the gas mass fraction within radius  $r < R_{*,90}$  and  $|z| < 2$  kpc from the disk mid-plane, of all our sample galaxies at different redshifts. In Figure 7, we present the mass fractions of all galaxies at redshift  $z_r = 0.0$  (top row),  $0.1$  (middle row) and  $1.0$  (bottom row). The left column shows the stellar mass fraction ( $M_*/M_{tot}$ ; orange circles), middle column is for DM mass fraction ( $M_{DM}/M_{tot}$ ; blue circles) and the right column is for the gas mass fraction ( $M_{gas}/M_{tot}$ ; green circles), where  $M_{tot}$  is the combined mass of all components. The dark-blue big solid circles show the median mass fraction in each panel and the shaded region is bounded by the 16<sup>th</sup> percentile and the 84<sup>th</sup> percentile curves.

As we move towards galaxies with higher bar strengths, the median value of the stellar mass fraction in the disk plane increases, the median of the DM mass fraction slightly decreases and the median gas mass fraction decreases to low values close to less than 5%. At high redshifts, the stellar mass fraction and gas fraction are higher than the low redshift values. At low redshifts, the DM mass fraction increases making the stellar and gas mass fractions lower. All the panels in Figure 7 reflect the well-established idea that stronger bars tend to last in galaxies with higher stellar mass fractions and lower gas mass fractions (Bland-Hawthorn et al. 2023).

Formation of a stellar bar depends on the stellar-to-dark matter mass ratio in the disk (Bland-Hawthorn et al. 2023), the kinematic coldness of the disk, gas fraction in the disk (Ostriker & Peebles 1973; Ansar et al. 2023b), strong satellite interaction events that trigger bar instability (Zana et al. 2018a,b; Rosas-Guevara et al.

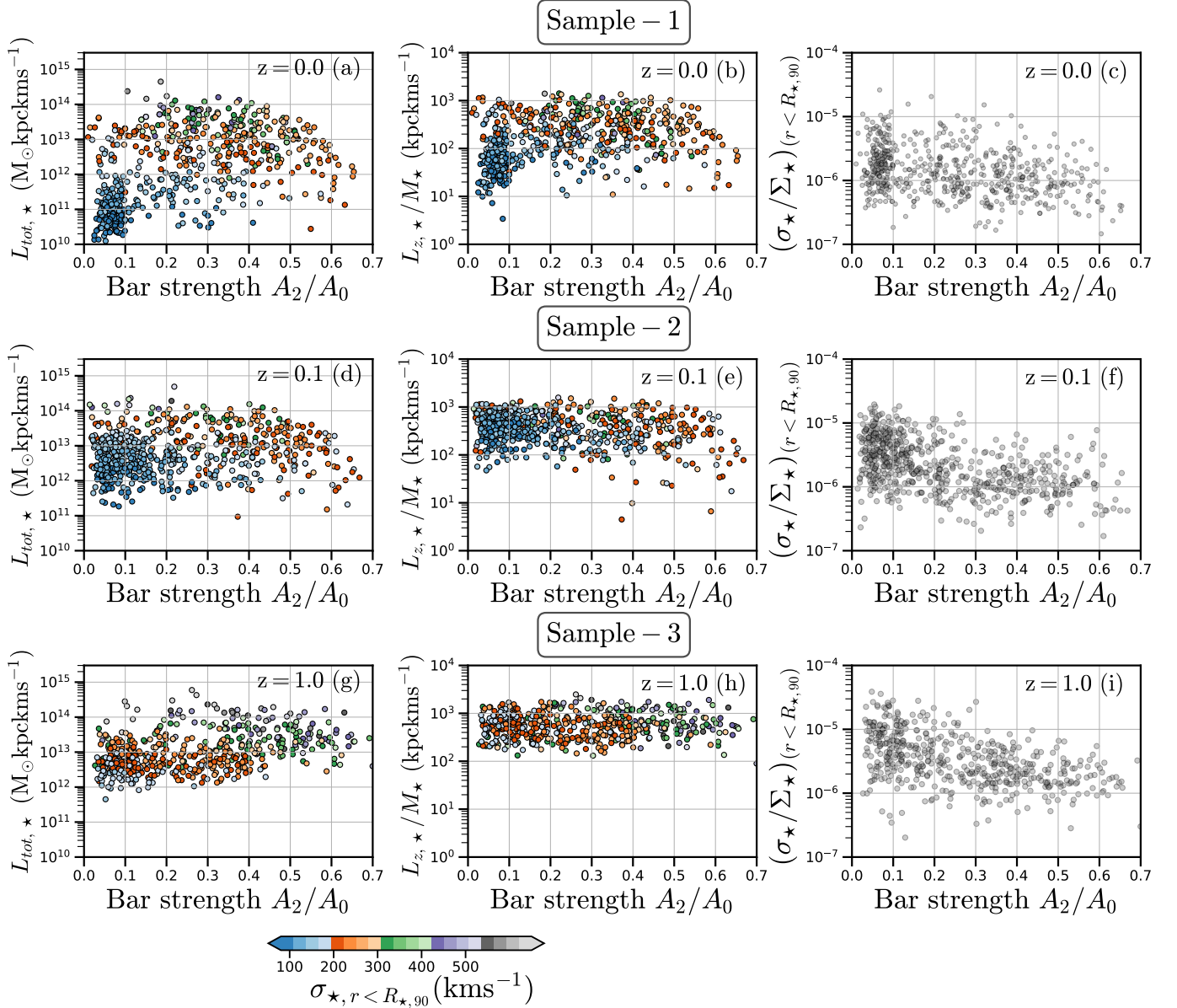


**Figure 6.** Stellar disk angular momentum ( $L_{tot}$ ; left column), specific angular momentum ( $L_{z,*}/M_*$ ; middle column) and the ratio of stellar dispersion to stellar surface density ( $\sigma_*/\Sigma_*$ ; right column) within spherical radius  $R_{*,90}$  for redshift  $z_r = 0.0$  (top row), 0.1 (middle row) and 1.0 (bottom row). Along with  $L_{tot}$  and  $L_{z,*}/M_*$  we show the stellar dispersion ( $\sigma_{*, r < R_{*,90}}$ ) with colors. Each bar strength group consists of stellar disks with a wide range of  $L_{tot}$ ,  $L_{z,*}/M_*$  and  $\sigma_*/\Sigma_*$  with no sign of strong trends. Galaxies at high redshifts have higher  $L_{tot}$ ,  $L_{z,*}/M_*$  and lower scatter in these quantities.

2022; Izquierdo-Villalba et al. 2022; Ansar et al. 2023b) and presence or absence of AGN activity (Zhou et al. 2020; Irodou et al. 2022; Kataria & Vivek 2023). However, in this article, we highlight that the connection between DM halos of low spin and the presence of strong bars in disks at present ( $z_r = 0.0$ ) is the result of cosmological evolution. We defer the detailed analysis of the origin of the inverse correlation between halo spin and bar instability (at  $z_r = 0.0$ ) to a subsequent article (Ansar et al. in prep).

## 5. DISCUSSION

We investigate the stellar bar - DM halo spin connection in disk galaxies from the TNG50 simulation (Nelson et al. 2019; Pillepich et al. 2019) at three different redshifts  $z_r = 0.0, 0.1$  and 1.0. First, we compare galaxies with similar DM halo mass (within radius  $r_m$ ) close to the baryonic disk, in the central regions of the galaxies. **We find at redshift  $z_r = 0.0$  there is an inverse correlation between the median**



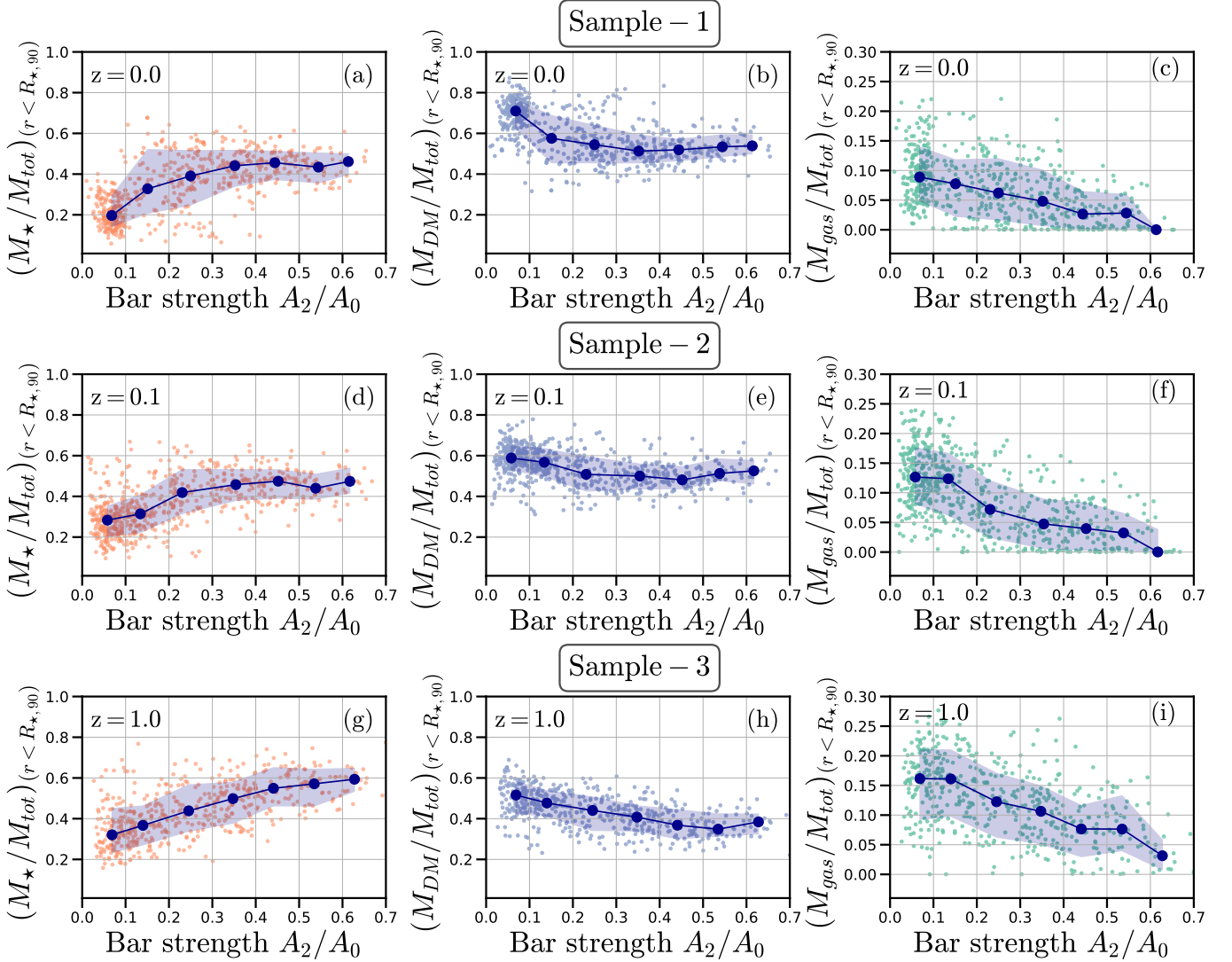


**Figure 7.** Stellar mass fraction ( $M_*/M_{tot}$ ; left column), dark matter mass fraction ( $M_{DM}/M_{tot}$ ; middle column) and gas mass fraction ( $M_{gas}/M_{tot}$ ; right column) at redshift  $z_r = 0.0$  (top row),  $0.1$  (middle row) and  $1.0$  (bottom row), within spherical radius  $R_{*,90}$  and  $|z| < 2$  kpc. In each panel, reddish/blue/green points are values of each quantity in different bar strength groups (Table 1). Blue lines connect the median values (dark blue circles) in each bar strength group and the shaded regions are bounded by the 16<sup>th</sup> and 84<sup>th</sup> percentile of each of the above quantities in each bar strength group.

**DM halo spin and the median bar strength.** The inverse correlation between median bar strength and median halo spin of galaxies is surprising, as in multiple studies with controlled isolated galaxy evolution (De-battista & Sellwood 2000; Athanassoula 2002; Kataria & Das 2019), DM halos are observed to gain angular momentum from the growth of bars. The above studies had adopted a fixed halo spin in all their DM models. However, recent studies by Li et al. (2023a,b) varied halo spin (at  $r_{vir}$ ) in different DM halo models and showed that halos with high spin ( $\lambda_B \sim 0.9$  at  $r_{vir}$ ) tend to absorb less angular momentum from the stellar disk compared to halos with low spin ( $\lambda_B \sim 0.0$  at  $r_{vir}$ ). For the TNG50 galaxies, we observe lower halo

spin/specific angular momentum, in the inner and the outer halo, for strongly barred galaxies compared to unbarred galaxies that show higher spin/specific angular momentum. However, a direct comparison between the final bar strength from Li et al. (2023a,b) and the TNG50 bars is out of scope of the current article, as the bars in Li et al. (2023a,b) evolve in isolation to undergo a buckling event that reduces the final bar strength for high spinning halos. Here we do not investigate buckling phenomena in our barred galaxy sample. Additionally, at higher redshifts ( $z_r = 1.0$ ) the inverse correlation does not hold, and we observe a more complex relation between halo spin and bar strength.



We also investigate the halo spin properties for three galaxy samples at the same redshifts without any constraints on halo mass. We find that the inverse correlation still holds for lower redshifts ( $z_r = 0$  and  $0.1$ ; not for  $z_r = 1$ ) and is more prominent for smaller radii close to the disk, compared to larger radii, closer to the virial radius of the DM halo where the difference between the median spin of the barred and unbarred galaxies decreases. In general, we find higher spinning halos at high redshift ( $z_r = 1$ ) compared to lower redshifts ( $z_r = 0.1$  and  $1$ ).

The bar-halo spin correlation evolves with time as the galaxy disks and their DM halos evolve. There could be multiple reasons behind the changing correlation between bar and halo spin. Mergers and flyby events of satellites can perturb the mass and velocity distribution of the DM halo (Rodriguez-Gomez et al. 2017). The characteristics of a satellite, for example, satellite mass (DM+baryonic), orbital inclination with the galaxy disk (prograde/retrograde/polar/in-plane), angular momentum of the incoming satellite can affect the DM halo mass and velocity distribution and hence the halo spin. The DM halo itself undergoes adiabatic contraction (Blumenthal et al. 1986; Kazantzidis et al. 2004; Gnedin et al. 2004), which can affect the halo spin distribution as it depends on the halo mass. The choice of the sample of galaxies to measure the halo spin can also affect the halo spin, as seen for Sample-1 (Section 4.1). For TNG50, low mass galaxies ( $M_*/M_\odot < 10^{10}$ ,  $M_{DM}/M_\odot < 10^{11}$ ) without any bar ( $A_2/A_0 < 0.2$ ) seems to have low halo spin compared to high mass galaxies (see Figure 10 in Appendix B). However, for low mass galaxies in TNG50 we also have to be cautious about the resolution at the central regions of these galaxies (Ansar et al. 2023a). Another disk component that we have not considered in our sample selection is the bulge mass and bulge spin. Bar formation is delayed for galaxies with massive bulges and even more delayed for high spinning bulges. Although, compared to the DM halo, the bulge plays a minor role in angular momentum exchange (Li et al. 2023b).

The DM halo angular momentum and the halo spin can also change due to angular momentum transfer from the disk to the DM halo through the stellar bar. A stellar bar can transfer angular momentum from the disk to the DM halo thereby increasing its strength and length, and decreasing its pattern speed (Debattista & Sellwood 2000). However, identifying the bar-halo angular momentum transfer in a cosmologically evolving galaxy is tricky, where multiple other external phenomena, for

example, satellite interactions, gas in-fall/out-flow, and internal phenomena, for example, stellar feedback and AGN activity, can as well modify the halo and disk angular momentum. Again, in a recent study with MW and M31-mass galaxies from the TNG50 simulations Khoperskov et al. (2023) showed that the disk formation time is early for strongly barred galaxies compared to weakly barred/unbarred galaxies. There is a possibility that for barred galaxies the early disk formation has provided enough time for the DM halo to lose halo spin, while for the unbarred galaxies (late disk formation), the halo spin did not get enough time to decrease.

We find that in the TNG50 simulations, as we move from high redshift to low redshifts the decrease in the median halo spin of barred galaxies is more compared to the unbarred galaxies. The evolution of halo spin suggests that, statistically, the evolutionary processes in galaxies lower the halo spin of barred galaxies more compared to weakly barred or unbarred galaxies. However, we do not expect the influence of the bar in the outer regions of galaxies. Still, we observe a slight anti-correlation between halo spin and bar strength at the outer radii as well. This indicates that the bar may not be responsible for the anti-correlation between bar strength and halo spin in the outer regions of DM halos. The formation of a strong bar may be the outcome of the evolution of DM halos with low outer halo spin. To uncover the origin of the inverse correlation between bar strength and halo spin, we plan to investigate the evolution of angular momentum in barred and unbarred galaxies in more detail in a future study (Ansar et al.).

The bar halo connection may have a significant impact on the origin of why about 2/3rds of the galaxies in our local Universe are barred. DM halos with low spin tend to host strongly barred galaxies at  $z_r = 0.0$ . However, whether this is a favourable condition for bar growth, we do not know yet. The halo spin values of barred and unbarred galaxies will contribute to the Universal halo spin distribution in different ways (Bullock et al. 2001). We have checked that the histogram of the halo spin of barred galaxies has a lower median halo spin compared to the spin distribution for unbarred galaxies (similar to Figure 4).

## 6. CONCLUSION

We investigate the stellar bar – DM halo spin connection in the TNG50 simulations at three different redshifts ( $z_r = 0.0, 0.1$  and  $1.0$ ) and find an inverse correlation between bar strength and halo spin for massive galaxies ( $M_* > 10^{10} M_\odot$ ) at low redshifts ( $z_r = 0.0$  and

0.1) but not at high redshifts ( $z_r = 1$ ). At low redshifts, galaxies hosting strong bars have DM halos of lower spin, lower angular momentum and lower specific angular momentum compared to unbarred galaxies. Whether the presence of the stellar bar decreases the inner dark matter halo spin or other internal/external processes lead to a decrease in halo spin, or is it related to early disk formation for the barred galaxies, remains to be investigated. The question of whether DM halos with low halo spin favour the growth of galaxies hosting a strong stellar bar has to be addressed with a detailed analysis of the evolution of galaxies in their cosmological environment using upcoming simulations.

We thank the IllustrisTNG Collaboration for making the TNG simulation data public and to be used widely by the community. The IllustrisTNG simulations were undertaken with compute time awarded by the Gauss Centre for Supercomputing (GCS) under GCS Large-Scale Projects GCS-ILLU and GCS-DWAR on the GCS share of the supercomputer Hazel Hen at the High Performance Computing Center Stuttgart (HLRS), as well as on the machines of the Max Planck Computing and Data Facility (MPCDF) in Garching, Germany. MD acknowledges the support of the Science and Engineering Research Board (SERB) MATRICS grant MTR/2020/000266 for this research.

## APPENDIX

### A. GALAXIES GROUPED IN TERMS OF BAR STRENGTH

Here we present the stellar mass, DM halo mass and gas mass of the galaxies from Sample 1, introduced in Section 2.1, for different bar strength bins from Table 1, in Figure 8.

### B. DECREASE OF HALO SPIN IN HIGHER BAR STRENGTH GALAXIES

We study the DM halo spin for comparable DM mass galaxies within the velocity range of  $200 < \text{Max}[V_{c,DM}(r < r_m)]/(\text{kms}^{-1}) < 250$  for  $r_m = 5$  and 10 kpc. We find 0, 6, 21, 23, 33, 8 and 0 number of galaxies for  $r_m = 10$  kpc for the seven bar strength ranges in Table 1 and similarly for  $r_m = 5$  kpc we have 0, 10, 19, 19, 17, 3 and 0 galaxies for each of the seven bar strength intervals. We avoid low statistics by considering the bar strength intervals with  $\geq 6$  galaxies. In Figure 9 we present the halo spin (panel a), halo angular momentum (panel b), halo mass (panel c) and halo spe-

*Software:* astropy (Astropy Collaboration et al. 2013, 2018), numpy (Harris et al. 2020), matplotlib (Hunter 2007)

cific angular momentum (panel d) for the above sample of barred and unbarred galaxies.

We also check the velocity range  $100 < \text{Max}[V_{c,DM}(r < r_m)]/(\text{kms}^{-1}) < 150$  with the low mass galaxies. However, we do not have uniform mass distribution for each of the bar strength intervals for the low mass systems. We find 72, 23, 38, 28, 8, 3 and 3 galaxies at  $r_m = 5$  kpc and 80, 27, 36, 22, 7, 2 and 2 galaxies for  $r_m = 10$  kpc. Again, we only consider the bar strength intervals with  $\geq 6$  galaxies. In Figure 10 we present the halo spin of the lowest mass galaxies for different bar strength intervals.

### C. ESTIMATION OF $R_{\star,60}$ , $R_{\star,90}$ AND $R_{200}$

The disk interacts with the DM halo through the stellar bar by transferring angular momentum from the disk to the inner DM halo. We aim to estimate the DM halo properties at scale lengths closely associated with the stellar disk. We estimate the radius of the 30%, 60% and 90% stellar mass within a spherical region of radius 30 kpc from the disk center,  $R_{\star,30}$ ,  $R_{\star,60}$  and  $R_{\star,90}$ .

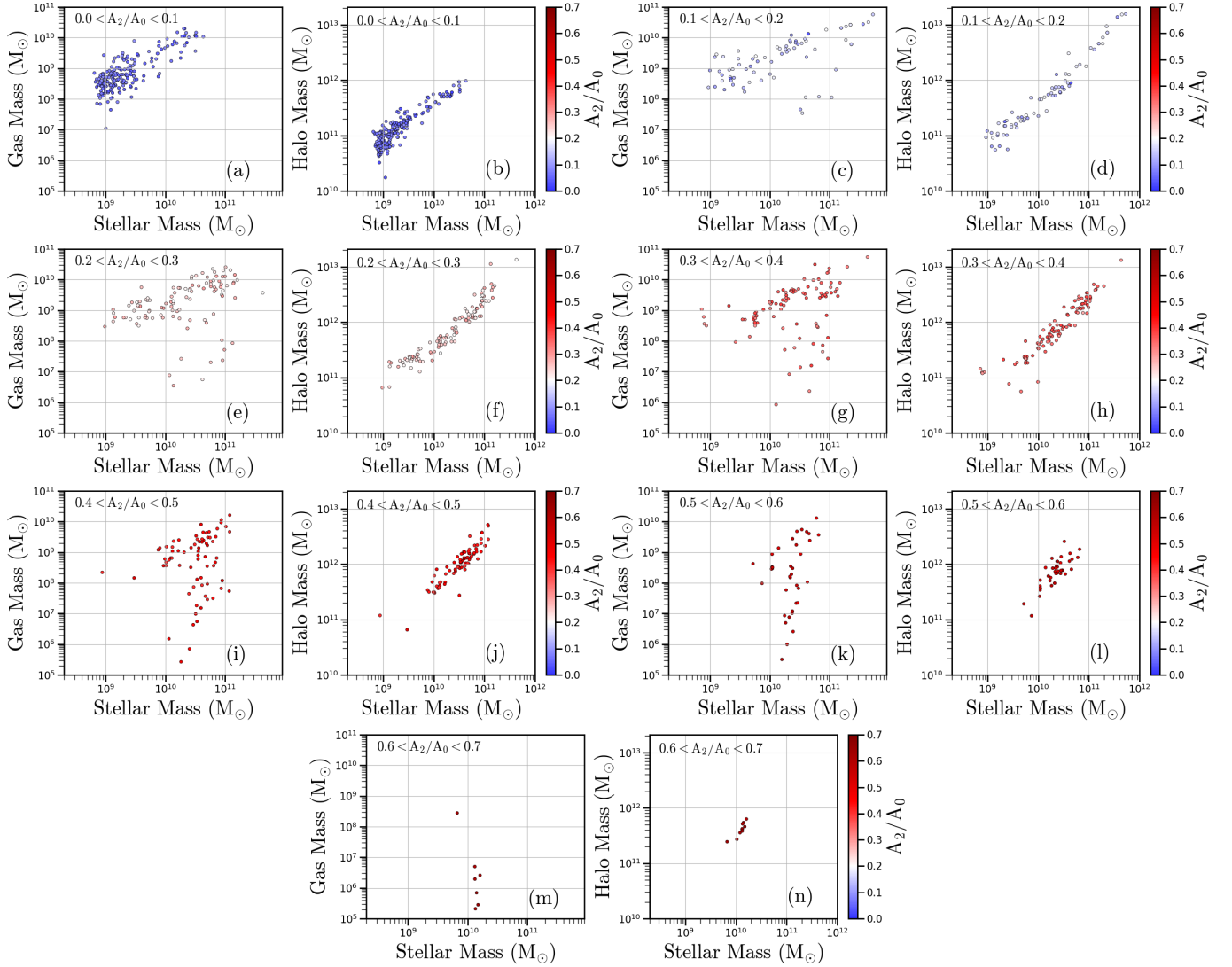


**Figure 8.** Barred ( $A_2/A_0 > 0.2$ , panel e-n) and unbarred ( $A_2/A_0 < 0.2$ , panel a-d) galaxies with different stellar mass, gas mass and DM mass at redshift  $z = 0$ . Galaxies with low gas mass show strongly barred systems. A large number of dwarf galaxies contribute to the unbarred sample (see panel a-d).

Most of the disks in our sample are well within the sphere of 30 kpc radius. Hence it is reasonable to estimate the radius containing 30%, 60% and 90% of the stellar mass within a sphere of radius 30 kpc. Some of the disks in our sample have small values of  $R_{*,30}$  and  $R_{*,60}$ , and estimation the DM halo properties at small radii can suffer from issues of numerical relaxation (Power et al. 2003). Following the method presented in Power et al. (2003), we estimate the radius that bounds the volume inside which the two-body relaxation time scale  $t_{relax}$  is smaller than the age of the Universe  $t_{age}$ . The radius at which  $t_{relax} = t_{age}$ , can be adopted as the radius of convergence ( $r_{conv}$ ) of the inner region of the DM halo.  $r_{conv}$  depends on the number of DM particles ( $N(< r)$ ), the mean density ( $\bar{\rho}(r)$ ) and the critical density of the Universe at redshift  $z_r$

( $\rho_{crit}(z_r) = 3H^2(z_r)/8\pi G$ ), and is a solution to the following equation:

$$\frac{t_{relax}}{t_{age}} = \frac{\sqrt{200}}{8} \frac{N(r)}{\ln N(r)} \left( \frac{\bar{\rho}(r)}{\rho_{crit}(z_r)} \right)^{-1/2} = 1. \quad (C1)$$

We solve the above equation for the radius of convergence  $r_{conv}$  in each of the galaxy DM in our samples and compare  $r_{conv}$  with  $R_{*,30}$ ,  $R_{*,60}$  and  $R_{*,90}$ . In Figure 11, where we show their comparison at two redshifts  $z_r = 0.0$  (first and second column for Sample-1) and 1.0 (third and fourth column for Sample-3). The first and third column show the comparison of  $R_{*,X}$  ( $X = 30, 60$  and 90) and  $r_{conv}$  and the black line marks the boundary of  $R_{*,X} = r_{conv}$ . The second and fourth columns show how  $r_{conv}$  varies with the bar strength of each galaxy from our samples. From visual inspection, the galax-

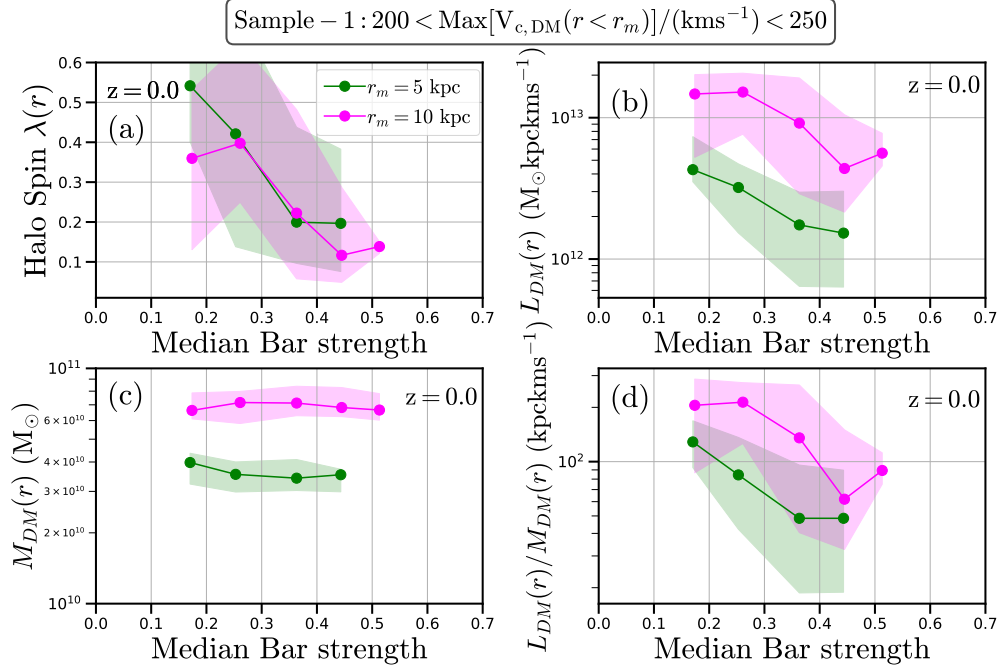


**Figure 9.** The anti-correlation between bar strength and dark matter halo spin at  $z_r = 0.0$ . Same as Figure 2, in the circular velocity range  $200 < \text{Max}[V_{c,DM}(r < r_m)]/(\text{kms}^{-1}) < 250$ .

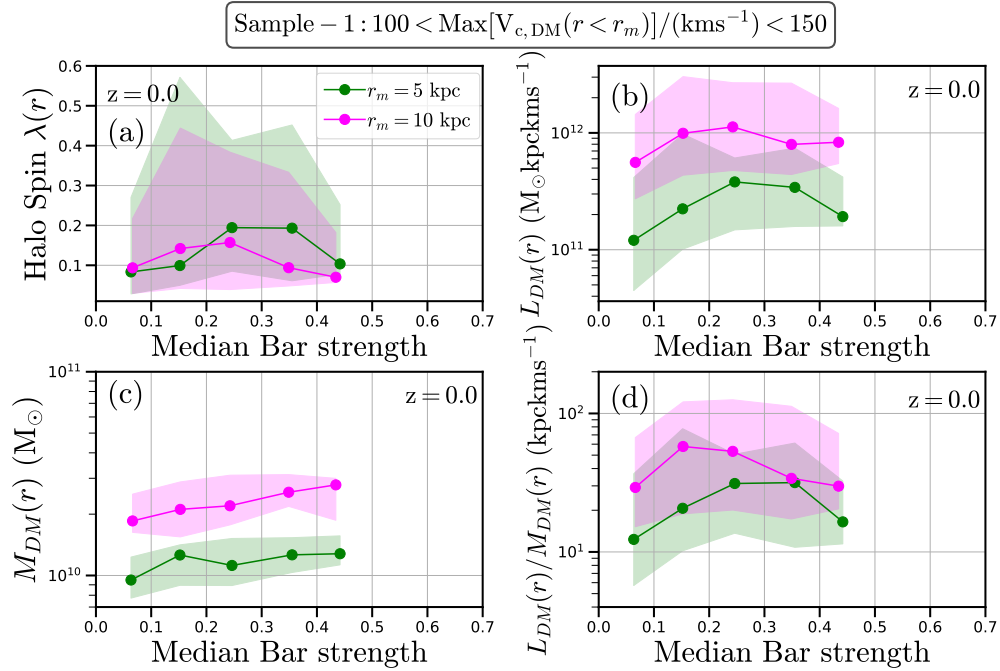


**Figure 10.** Similar to Figure 2, in the circular velocity range  $100 < \text{Max}[V_{c,DM}(r < r_m)]/(\text{kms}^{-1}) < 150$ .

ies in green and blue seem to be uniformly distributed throughout the bar strength range. In Figure 11 in all panels, each circle represent a galaxy from our Samples 1 and 3.

The convergence criteria is fulfilled by the galaxies shown in green for which  $R_{*,X} > r_{conv}$  (percentage of galaxies shown inside panels), and not by the galaxies shown in blue where  $R_{*,X} < r_{conv}$ . At  $R_{*,30}$ , less number of galaxies follow the above criteria compared to  $R_{*,90}$ . To ensure numerical convergence for the majority of the sample, we choose galaxies with  $R_{*,X} > r_{conv}$  and estimate the halo properties at  $R_{*,60}$  and  $R_{*,90}$ . This ensures that we have a sufficient number of galaxies in our samples to estimate halo properties and also avoid issues related to the numerical relaxation of DM particles.

Till now we have focused on length scales associated with the stellar disk that can be useful to measure DM halo spin. However, we also want to study the halo spin at different halo radii, for example, the virial radius  $R_{200}$ .  $R_{200}$  is defined as the radius inside which the

average density is 200 times the critical density of the Universe:

$$M_{200} = \frac{4}{3}\pi R_{200}^3 \times (200\rho_{crit}(z_r)) \quad (C2)$$

where,  $M_{200}$  is the virial mass and  $\rho_{crit}(z_r) = 3H^2(z_r)/8\pi G$  is the critical density at redshift  $z_r$ . We estimate the average density at different radii and a match with  $200 \times \rho_{crit}(z_r)$  gives  $R_{200}$ . To study the effect of the disk we measure the halo spin at  $R_{200}$  away from the influence of the stellar disk, and at radii closer to the disk -  $0.15R_{200}$  and  $0.05R_{200}$ .

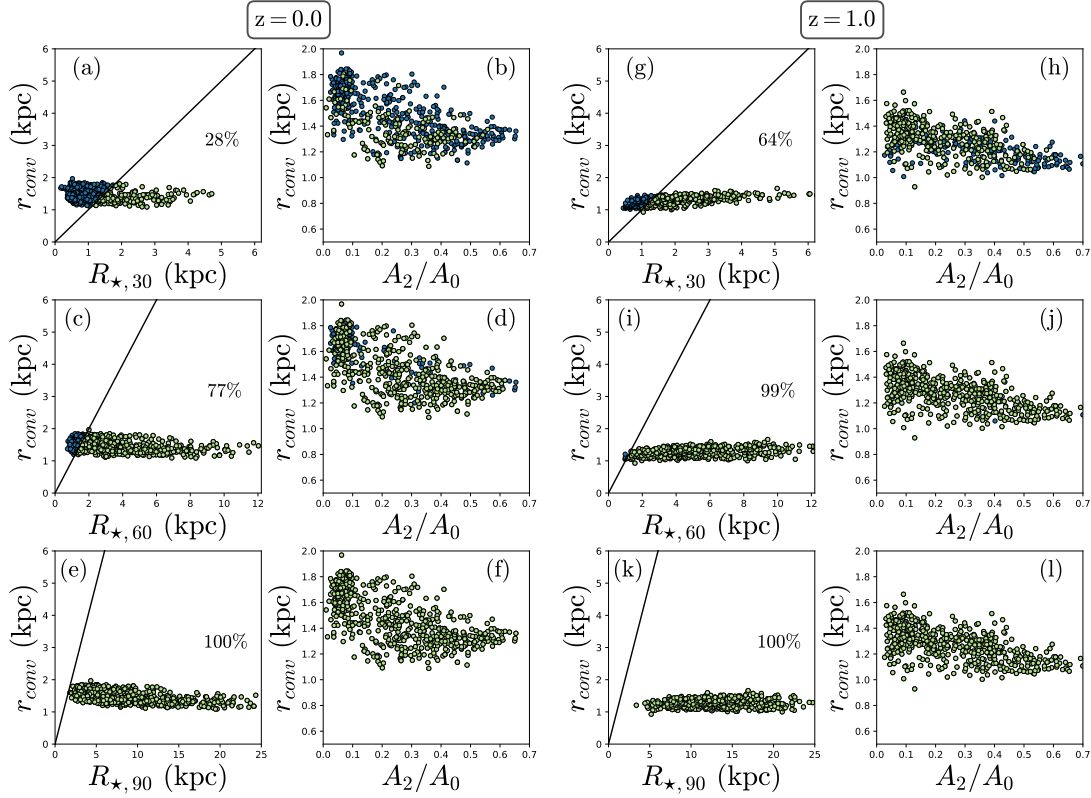
#### D. BARYON FRACTION IN THE DISK WITHIN $R_{*,90}$

Figure D shows the fraction of baryonic mass in the gaseous component  $M_{gas}/(M_{gas} + M_*)$  and in the stellar component  $M_*/(M_{gas} + M_*)$  in the disk plane (within  $r < R_{*,90}$  and  $|z| < 2$  kpc) for all the galaxies in the three Samples from Table 1 for different bar strength ( $A_2/A_0$ ) groups.

## REFERENCES

- Ansar, S., Kataria, S. K., & Das, M. 2023a, MNRAS, 522, 2967, doi: [10.1093/mnras/stad1060](https://doi.org/10.1093/mnras/stad1060)
- Ansar, S., Pearson, S., Sanderson, R. E., et al. 2023b, arXiv e-prints, arXiv:2309.16811, doi: [10.48550/arXiv.2309.16811](https://doi.org/10.48550/arXiv.2309.16811)
- Astropy Collaboration, Robitaille, T. P., Tollerud, E. J., et al. 2013, A&A, 558, A33, doi: [10.1051/0004-6361/201322068](https://doi.org/10.1051/0004-6361/201322068)
- Astropy Collaboration, Price-Whelan, A. M., Sipőcz, B. M., et al. 2018, AJ, 156, 123, doi: [10.3847/1538-3881/aabc4f](https://doi.org/10.3847/1538-3881/aabc4f)
- Athanassoula, E. 2002, ApJL, 569, L83, doi: [10.1086/340784](https://doi.org/10.1086/340784)
- . 2003, MNRAS, 341, 1179, doi: [10.1046/j.1365-8711.2003.06473.x](https://doi.org/10.1046/j.1365-8711.2003.06473.x)
- Athanassoula, E., & Misiriotis, A. 2002, MNRAS, 330, 35, doi: [10.1046/j.1365-8711.2002.05028.x](https://doi.org/10.1046/j.1365-8711.2002.05028.x)
- Barnes, J., & Efstathiou, G. 1987, ApJ, 319, 575, doi: [10.1086/165480](https://doi.org/10.1086/165480)
- Bett, P., Eke, V., Frenk, C. S., et al. 2007, MNRAS, 376, 215, doi: [10.1111/j.1365-2966.2007.11432.x](https://doi.org/10.1111/j.1365-2966.2007.11432.x)
- Bett, P., Eke, V., Frenk, C. S., Jenkins, A., & Okamoto, T. 2010, MNRAS, 404, 1137, doi: [10.1111/j.1365-2966.2010.16368.x](https://doi.org/10.1111/j.1365-2966.2010.16368.x)
- Bett, P. E., & Frenk, C. S. 2012, MNRAS, 420, 3324, doi: [10.1111/j.1365-2966.2011.20275.x](https://doi.org/10.1111/j.1365-2966.2011.20275.x)
- . 2016, MNRAS, 461, 1338, doi: [10.1093/mnras/stw1395](https://doi.org/10.1093/mnras/stw1395)
- Bland-Hawthorn, J., Tepper-Garcia, T., Agertz, O., & Freeman, K. 2023, ApJ, 947, 80, doi: [10.3847/1538-4357/acc469](https://doi.org/10.3847/1538-4357/acc469)
- Blumenthal, G. R., Faber, S. M., Flores, R., & Primack, J. R. 1986, ApJ, 301, 27, doi: [10.1086/163867](https://doi.org/10.1086/163867)
- Bullock, J. S., Dekel, A., Kolatt, T. S., et al. 2001, ApJ, 555, 240, doi: [10.1086/321477](https://doi.org/10.1086/321477)
- Collier, A., & Madigan, A.-M. 2021, ApJ, 915, 23, doi: [10.3847/1538-4357/ac004d](https://doi.org/10.3847/1538-4357/ac004d)
- Collier, A., Shlosman, I., & Heller, C. 2018, MNRAS, 476, 1331, doi: [10.1093/mnras/sty270](https://doi.org/10.1093/mnras/sty270)
- . 2019a, MNRAS, 488, 5788, doi: [10.1093/mnras/stz2144](https://doi.org/10.1093/mnras/stz2144)
- . 2019b, MNRAS, 489, 3102, doi: [10.1093/mnras/stz2327](https://doi.org/10.1093/mnras/stz2327)
- Debattista, V. P., & Sellwood, J. A. 2000, ApJ, 543, 704, doi: [10.1086/317148](https://doi.org/10.1086/317148)
- Doroshkevich, A. G. 1970, Astrophysics, 6, 320, doi: [10.1007/BF01001625](https://doi.org/10.1007/BF01001625)
- Efstathiou, G., Lake, G., & Negroponte, J. 1982, MNRAS, 199, 1069, doi: [10.1093/mnras/199.4.1069](https://doi.org/10.1093/mnras/199.4.1069)
- Gnedin, O. Y., Kravtsov, A. V., Klypin, A. A., & Nagai, D. 2004, ApJ, 616, 16, doi: [10.1086/424914](https://doi.org/10.1086/424914)
- Harris, C. R., Millman, K. J., van der Walt, S. J., et al. 2020, Nature, 585, 357, doi: [10.1038/s41586-020-2649-2](https://doi.org/10.1038/s41586-020-2649-2)
- Hunter, J. D. 2007, Computing in Science & Engineering, 9, 90, doi: [10.1109/MCSE.2007.55](https://doi.org/10.1109/MCSE.2007.55)
- Irodotou, D., Fragkoudi, F., Pakmor, R., et al. 2022, MNRAS, 513, 3768, doi: [10.1093/mnras/stac1143](https://doi.org/10.1093/mnras/stac1143)





**Figure 11.** Comparison of  $R_{*,60}$  and  $R_{*,90}$  with the radius of convergence  $r_{conv}$  at redshift  $z_r = 0.0$  (first and second column) and 1.0 (third and fourth column). First and third column shows  $R_{*,X}$  ( $X = 60$  and  $90$ ) versus  $r_{conv}$  (see text in Appendix C), and second and fourth column shows  $r_{conv}$  versus bar strength  $A_2/A_0$  for the same galaxies. The green circles represent galaxies with  $R_{*,X} > r_{conv}$  and the blue circles for galaxies with  $R_{*,X} < r_{conv}$ . The percentage of green circles is shown in the different panels. As we move from  $R_{*,60}$  to  $R_{*,90}$  the fraction of galaxies satisfying the numerical convergence ( $R_{*,X} > r_{conv}$ ) increases to 100% for  $R_{*,90}$  at all redshifts.

Izquierdo-Villalba, D., Bonoli, S., Rosas-Guevara, Y., et al. 2022, MNRAS, 514, 1006, doi: [10.1093/mnras/stac1413](https://doi.org/10.1093/mnras/stac1413)  
Jang, D., & Kim, W.-T. 2023, ApJ, 942, 106, doi: [10.3847/1538-4357/aca7bc](https://doi.org/10.3847/1538-4357/aca7bc)  
Jiang, F., Dekel, A., Kneller, O., et al. 2019, MNRAS, 488, 4801, doi: [10.1093/mnras/stz1952](https://doi.org/10.1093/mnras/stz1952)  
Kataria, S. K., & Das, M. 2018, MNRAS, 475, 1653, doi: [10.1093/mnras/stx3279](https://doi.org/10.1093/mnras/stx3279)  
—. 2019, ApJ, 886, 43, doi: [10.3847/1538-4357/ab48f7](https://doi.org/10.3847/1538-4357/ab48f7)  
Kataria, S. K., & Shen, J. 2022, ApJ, 940, 175, doi: [10.3847/1538-4357/ac9df1](https://doi.org/10.3847/1538-4357/ac9df1)  
Kataria, S. K., & Vivek, M. 2023, MNRAS, doi: [10.1093/mnras/stad3383](https://doi.org/10.1093/mnras/stad3383)  
Kazantzidis, S., Kravtsov, A. V., Zentner, A. R., et al. 2004, ApJL, 611, L73, doi: [10.1086/423992](https://doi.org/10.1086/423992)  
Khoperskov, S., Minchev, I., Steinmetz, M., et al. 2023, arXiv e-prints, arXiv:2309.07321, doi: [10.48550/arXiv.2309.07321](https://doi.org/10.48550/arXiv.2309.07321)  
Kim, J.-h., & Lee, J. 2013, MNRAS, 432, 1701, doi: [10.1093/mnras/stt632](https://doi.org/10.1093/mnras/stt632)

Li, X., Shlosman, I., Heller, C., & Pfenniger, D. 2023a, MNRAS, 526, 1972, doi: [10.1093/mnras/stad2799](https://doi.org/10.1093/mnras/stad2799)  
Li, X., Shlosman, I., Pfenniger, D., & Heller, C. 2023b, arXiv e-prints, arXiv:2310.01411, doi: [10.48550/arXiv.2310.01411](https://doi.org/10.48550/arXiv.2310.01411)  
Long, S., Shlosman, I., & Heller, C. 2014, ApJL, 783, L18, doi: [10.1088/2041-8205/783/1/L18](https://doi.org/10.1088/2041-8205/783/1/L18)  
Maller, A. H., Dekel, A., & Somerville, R. 2002, MNRAS, 329, 423, doi: [10.1046/j.1365-8711.2002.04983.x](https://doi.org/10.1046/j.1365-8711.2002.04983.x)  
Marioni, O. F., Abadi, M. G., Gottlöber, S., & Yepes, G. 2022, MNRAS, 511, 2423, doi: [10.1093/mnras/stac105](https://doi.org/10.1093/mnras/stac105)  
Nelson, D., Pillepich, A., Springel, V., et al. 2019, MNRAS, 490, 3234, doi: [10.1093/mnras/stz2306](https://doi.org/10.1093/mnras/stz2306)  
Ostriker, J. P., & Peebles, P. J. E. 1973, ApJ, 186, 467, doi: [10.1086/152513](https://doi.org/10.1086/152513)  
Peebles, P. J. E. 1969, ApJ, 155, 393, doi: [10.1086/149876](https://doi.org/10.1086/149876)  
Pérez-Montaño, L. E., Rodríguez-Gómez, V., Cervantes Sodi, B., et al. 2022, MNRAS, 514, 5840, doi: [10.1093/mnras/stac1716](https://doi.org/10.1093/mnras/stac1716)

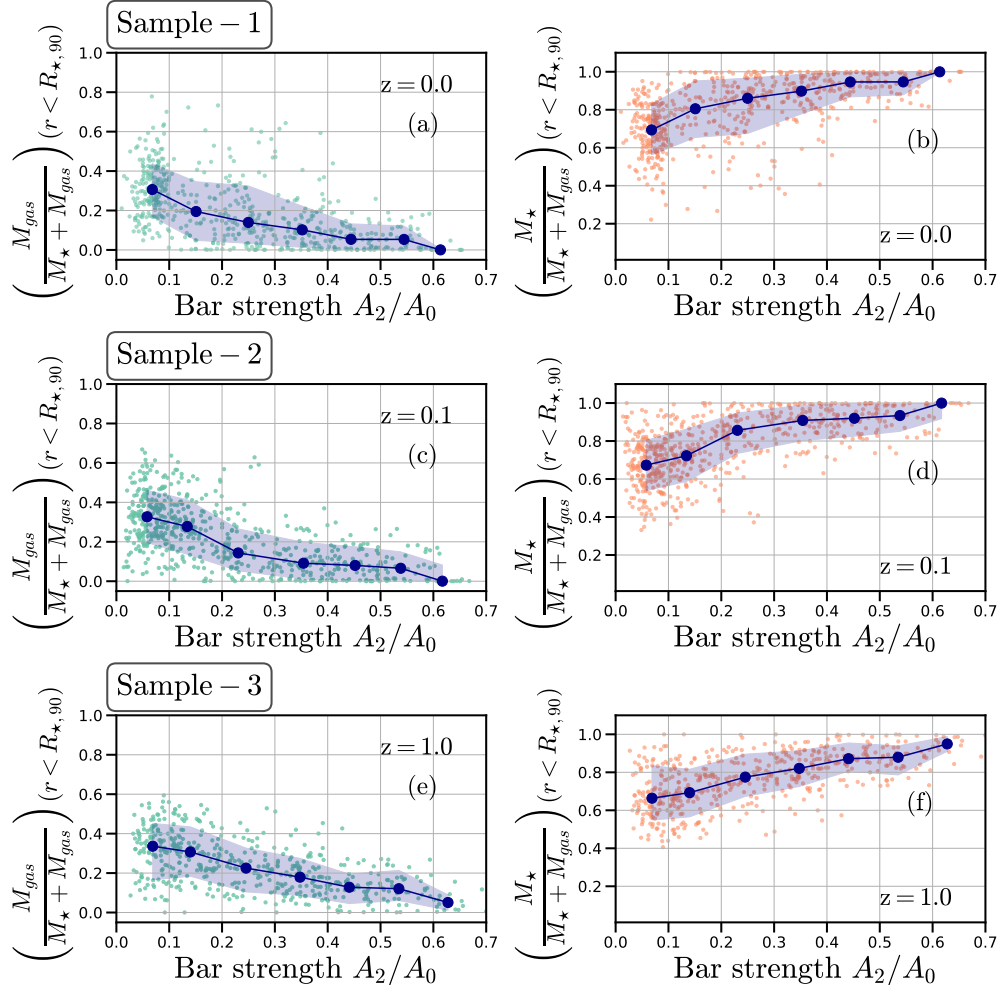


**Figure 12.** Higher bar strength galaxies have higher fraction of stellar mass and lower fraction of gas mass in the disk plane ( $|z| < 2$  kpc) within a radius of  $R_{\star,90}$ .

Pillepich, A., Springel, V., Nelson, D., et al. 2018, MNRAS, 473, 4077, doi: [10.1093/mnras/stx2656](https://doi.org/10.1093/mnras/stx2656)  
Pillepich, A., Nelson, D., Springel, V., et al. 2019, MNRAS, 490, 3196, doi: [10.1093/mnras/stz2338](https://doi.org/10.1093/mnras/stz2338)  
Power, C., Navarro, J. F., Jenkins, A., et al. 2003, MNRAS, 338, 14, doi: [10.1046/j.1365-8711.2003.05925.x](https://doi.org/10.1046/j.1365-8711.2003.05925.x)  
Rodríguez-Gómez, V., Sales, L. V., Genel, S., et al. 2017, MNRAS, 467, 3083, doi: [10.1093/mnras/stx305](https://doi.org/10.1093/mnras/stx305)  
Rodríguez-Gómez, V., Genel, S., Fall, S. M., et al. 2022, MNRAS, 512, 5978, doi: [10.1093/mnras/stac806](https://doi.org/10.1093/mnras/stac806)  
Romeo, A. B., Agertz, O., & Renaud, F. 2023, MNRAS, 518, 1002, doi: [10.1093/mnras/stac3074](https://doi.org/10.1093/mnras/stac3074)  
Rosas-Guevara, Y., Bonoli, S., Dotti, M., et al. 2022, MNRAS, 512, 5339, doi: [10.1093/mnras/stac816](https://doi.org/10.1093/mnras/stac816)  
Saha, K., & Naab, T. 2013, MNRAS, 434, 1287, doi: [10.1093/mnras/stt1088](https://doi.org/10.1093/mnras/stt1088)  
Schäfer, B. M. 2009, International Journal of Modern Physics D, 18, 173, doi: [10.1142/S0218271809014388](https://doi.org/10.1142/S0218271809014388)  
Sellwood, J. A. 2014, Reviews of Modern Physics, 86, 1, doi: [10.1103/RevModPhys.86.1](https://doi.org/10.1103/RevModPhys.86.1)

Springel, V. 2010, MNRAS, 401, 791, doi: [10.1111/j.1365-2966.2009.15715.x](https://doi.org/10.1111/j.1365-2966.2009.15715.x)  
Vitvitska, M., Klypin, A. A., Kravtsov, A. V., et al. 2002, ApJ, 581, 799, doi: [10.1086/344361](https://doi.org/10.1086/344361)  
Weinberger, R., Springel, V., Hernquist, L., et al. 2017, MNRAS, 465, 3291, doi: [10.1093/mnras/stw2944](https://doi.org/10.1093/mnras/stw2944)  
White, S. D. M. 1984, ApJ, 286, 38, doi: [10.1086/162573](https://doi.org/10.1086/162573)  
Yang, H., Gao, L., Frenk, C. S., et al. 2023, MNRAS, 518, 5253, doi: [10.1093/mnras/stac3335](https://doi.org/10.1093/mnras/stac3335)  
Zana, T., Dotti, M., Capelo, P. R., et al. 2018a, MNRAS, 473, 2608, doi: [10.1093/mnras/stx2503](https://doi.org/10.1093/mnras/stx2503)  
—. 2018b, MNRAS, 479, 5214, doi: [10.1093/mnras/sty1850](https://doi.org/10.1093/mnras/sty1850)  
Zhou, Z.-B., Zhu, W., Wang, Y., & Feng, L.-L. 2020, ApJ, 895, 92, doi: [10.3847/1538-4357/ab8d32](https://doi.org/10.3847/1538-4357/ab8d32)  
Zjupa, J., & Springel, V. 2017, MNRAS, 466, 1625, doi: [10.1093/mnras/stw2945](https://doi.org/10.1093/mnras/stw2945)